NTNU

Norwegian University of
Science and Technology

Construction of Nanocellulose Microcapsules for Research and Sensor Applications

Sandra Karen Tonstad

Nanotechnology
Submission date: June 2018
Supervisor: Kristin Syverud, IKP
Co-supervisor: Vegar Ottesen, IKP

Norwegian University of Science and Technology
Department of Chemical Engineering

The art and science of asking questions is the source of all knowledge.

—Thomas Berger, Novelist

Abstract

Nanocellulose microcapsules with internal hollows have previously been found to form when cellulose nanofibrils (CNF) are added to paper pulp before drying. In an effort to study such capsules removed from the paper matrix, attempts have been made to develop a production protocol using a aqueous layer-by-layer (LbL) technique. Studying the capsules separately is theorized to expose interesting interface properties as well as provide an opportunity for creation of sensors for use in gaseous environments. Before such possibilities can be investigated, capsules formation must be established. TEMPO-oxidized nanofibrilated cellulose (CNF-T) in combination with PDADMAC were adsorbed around central $CaCO_3$ template particles to form the polyelectrolyte layers. Investigation into the use of freeze-drying with liquid N_2 as coolant was done to confirmed this as a viable method for drying the resulting structures. The structures were studied using scanning electron microscopy (SEM), alone or in combination with focused ion beam (FIB) milling. ζ-potential measurements show that the alternating layers began forming. Other techniques such as scanning transmission electron microscopy (STEM), optical microscopy and light scattering were also used. Characterization of the starting materials showed the template particles to have an average diameter of $\sim 6.3\,\mu\mathrm{m}$. The CNF-T fibrils were determined to have an average diameter of $\sim 2.7\,\mathrm{nm}$ and rheological studies revealed a critical overlap concentration of 0.17% (w/w). The process described in this work provides a first step towards creating layered capsules of CNF-T for use in further research.

Sammendrag

Nanocellulosemikrokapsler med interne hulrom har tidligere blitt oppdaget når nanofibriller av cellulose blir tilsatt papirmasse før tørking. For å kunne studere slike kapsler utenfor det tørre papiret, er det fokus på å prøve å lage en fungerende prosess for å lage kapsler ved bruk av en lag-på-lag (LBL) teknikk. Ved å studere kapslene utenfor papirmatrisen kan det teoretisk sett være mulig å avdekke interessant egenskaper i tillegg til å skape fremtidige muligheter for å lage sensorer til bruk med gass. Før det er mulig å utforske slike muligheter, må det etableres en metode for å fremstille kapsler. TEMPO-oksiderte nanocellulosefibriller kombinert med PDADMAC adsorberte lagvis på overflaten av en sentral $CaCO_3$ partikkel. Frysetørking med flytende N_2 som kjølemiddel ble bekreftet som en mulighet for å tørke de resulterende strukturene. Strukturene ble caracterisert ved hjelp av sveipeelectronmikriskop (SEM), alene eller i kombinasjon med fokusertionestrålemølling (FIB). ζ-potensialmålinger ble brukt for å bekrefte lagdannelse. Teknikker som sveipetransmisjonsmikroskopi (STEM), optisk mikroskopi og lysspredning ble også tatt i bruk. Karakterisering av startmaterialene avdekket at $CaCO_3$ partiklene hadde en gjennomsnittlig diameter på $\sim 6.3\,\mu\mathrm{m}$. Nanofibrillene viste seg å ha en diameter på $\sim 2.7\,\mathrm{nm}$, og en kritisk overlapskonsentrasjon på 0.17% (v/v) ble oppdaget ved hjelp av reologiske studier. Prosessen beskrevet i dette arbeidet er et første steg på vei mot å lage ferdige nanocellulosemikrokapsler til bruk i fremtidig forskning.

Preface

This work is submitted in fulfillment of requirements for a M.Sc degree in Nanotechnology at the Norwegian University of Science and Technology (NTNU). The work has been carried out the Department of Chemical Engineering at NTNU, with Adjunct Professor Kristin Syverud at NTNU and RISE PFI as the main supervisor and Dr. Vegar Ottesen as co-supervisor. Experimental work has been performed at the Environmental Engineering and Reactor Technology group, Ugelstad laboratories, NTNU Nanolab cleanroom facilities and the Paper and Fiber research institute (PFI).

Acknowledgments

The work needed to get to this point could not have been done without the help of several people. I would first like to thank my supervisor Professor Kristin Syverud for her guidance throughout the year. The most sincere thanks are extended to my co-supervisor Dr. Vegar Ottesen for his invaluable assistance, encouragement and dedication. Without which this year would not have been such a rewarding one.

Many thanks are extended to RISE PFI for access to their laboratories, as well as to their staff. In particular Inbebjørg Leirset for her guidance in the laboratory, Per Olav Johnsen for sharing his knowledge on sample preparation and Birgitte Hjelmeland McDonagh for rewarding and interesting discussions about my work and for sharing with me her insights into microscopy and polymers.

To the Ugelstad Laboratory and staff, I am deeply thankful for opening their laboratories to me and for providing training and answering questions. Additionally, Gøril Flatberg deserves thanks for making herself available to me for training and access to liquid nitrogen. So too does Jonathan Økland Torstensen for giving me prior access to his recently published paper, and guiding me in the techniques contained therein.

NTNU Nanolab and Norfab are thanked abundantly for the opportunity to work in a top notch laboratory. Special thanks are due Erik Roede and Aleksander Mosberg for sharing invaluable insights into FIB.

To my family and friends. I would like to thank you all so much for keeping my head up for me when it sagged, and always being there with a hug. To Mom and Pappa in particular, thank you so much for answering to the best of your abilities my multitude of questions while growing up. And for always believing in your smart cookie.

Table of Contents

List of Tables

List of Figures

Acronyms

AFM atomic force microscopy. xiii, xiv, 17, 18, 40, 52, 54, 74

BF bright field. xiii, 26, 34, 38, 42, 43

BSE backscatter electron. 19–21, 24, 62

CNF cellulose nanofibrils. i, ix, 1, 2, 5, 10, 53, 61, 62

CNF-T TEMPO-oxidized cellulose nanofibrils. i, xi, xiii, xiv, 2, 32–34, 40–47, 52–64, 73, 74

D[3,2] surface area moment mean diameter. 13, 38, 50

D[4,3] volume or mass moment mean diameter. 13, 32, 37, 42, 43, 49, 50

DF dark field. xiv, 26, 34, 45, 56, 58, 59

DI deionized. 31, 33

DIC differential interface contrast. xiii, 16, 34, 42, 43

EDX energy dispersive X-ray spectroscopy. xiii, 25, 26, 43, 44, 58

ETD Everhart-Thornly detector. 35, 44, 47, 57, 59

FIB focused ion beam. i, xiv, 3, 27, 29, 34, 38, 45, 48, 58–60

ICE in-column electron detector. 35, 39, 47, 57

LbL layer-by-layer. i, 3, 6

LMIS liquid-metal ion source. 27

MC Monte Carlo. 27

PCC precipitated calcium carbonate. xiii, xiv, 2, 3, 32, 33, 35, 38, 39, 42–47, 49–51, 54–63

PDADMAC polydiallyldemethylammonium chloride. i, 2, 32–34, 42, 49, 50, 55, 58, 59, 61, 63

PEM polyelectrolyte multilayer. 1, 6, 55, 61–63

RCF relative centrifugal force. 14, 15

SD standard deviation. 37, 41, 73

SE secondary electron. xiii, 19–22, 24, 35, 38, 39, 44–48, 51, 56, 57, 59, 60, 62

SEM scanning electron microscopy. i, xiii, xiv, 3, 19, 23, 26, 27, 34, 37, 38, 44–46, 50, 56, 58–60, 62

SIM secondary ion microscopy. 27, 29

STEM scanning tunneling electron microscopy. i, xiv, 3, 26, 34, 45, 56, 60, 62

TEM transmission electron microscopy. 26, 34, 52, 62

TEMPO 2,2,6,6-tetramethypireperidine-1-oxyl. 5, 61

TLD through lense detector. 35, 45, 47, 48, 51

WD working distance. 20

Chapter 1

Introduction

Sensors are an integral part of modern life. They can be found in almost all everyday objects with any electronic capacity, providing constant feedback about their environment. Advances in semiconductor manufacturing, has been a large contributor to this [1]. Work is continually being done to find new sensors aimed at sensing in new environments. Delving into biology, sensors in this field are required to work in conditions where traditional electronics may not be of use. Using viral capsid proteins has been studied extensively [2–5]. Capsid proteins have the ability to self assemble [6, 7], and can further encapsulate desired molecules or nanoscopic particles [8–10]. Functionalizing either the outer of inner surfaces of the self assembled structure yields sensors enabling protein detection [11], strains sensing [12], and cancer detection [10], to mention a few. Virus capsid proteins are sensitive to several environmental factors and most specifically to pH [2, 9, 13], adding a useful tunability.

It is clear that there is abundant research on virus capsid protein as sensors, and while these sensors may be very useful they are all based on use in liquid environments. The tunable permeability of cellulose nanofibrils (CNF) in response to moisture is one of the properties making this material interesting in general [14], but also more specifically as sensor material. Loading vessels made from CNF, in much the same way as were the capsid shells or polyelectrolyte multilayer (PEM) capsules [15–19], opens the possibility of creating sensors for use in gaseous environments.

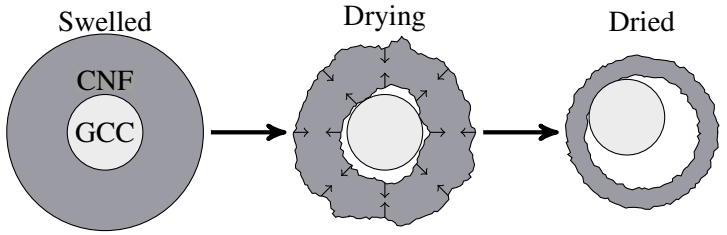

Figure 1.1: Illustrating the hypothesized process of CNF-T capsule formation upon drying. Contact with $CaCO_3$ (GCC) is retained only along a portion of the particle. Reprinted from [20] with permission.

Research is being done to incorporate nanocellulose into paper matrix as well as employing CNF in films [20, 21]. In part the interest is due to their excellent - some would say superior - barrier properties [22, 23]. This and the work done by Ottesen et al. (2017) is the inspiration for this study [20]. Ottesen et al. discovered that when CNF was added to paper matrix the CNF accumulated as capsules around $CaCO_3$ particles (denoted GCC). Upon drying separation of the CNF from the $CaCO_3$ core was observed, creating a hollow cavity. An illustration of this is found in Figure 1.1. This project is aimed at replicating the aforementioned effect by preparing the capsules in solution, thus in effect removing the capsules from the paper matrix.

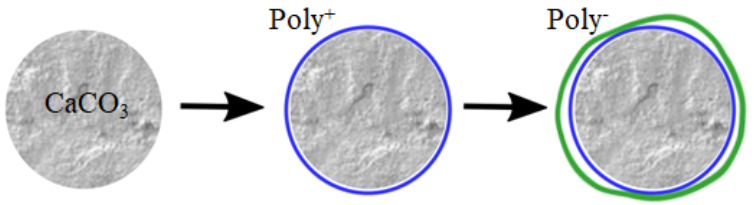

Figure 1.2: Illustrating the process of building layers of positively charged polymer (blue) and CNF-T (green) around a particle of $CaCO_3$

The main aim of this work is therefore to produce PEM capsules of poly(diallyldimethylammonium chloride) (PDADMAC) and TEMPO-oxidized cellulose nanofibrils (CNF-T) around a central template particle, here precipitated calcium carbonate (PCC) - illustrated in Figure 1.2. If the capsules can be studied outside a paper matrix, this might shed light on the optical properties of the paper matrix by separately looking at the interfaces in the material [21, 24], and can help increase understanding of how CNF behaves in concert with other materials. The capsules may further be used in the research and sensor capacities detailed above.

Construction is attempted through a layer-by-layer (LbL) process using the surfaces charges of the PCC and polymers. Working in surface charge excess with multiple centrifugation steps, the first layer is added and the excess is washed away [25–27]. Surface area calculations provide more exact amounts of polymer needed for coverage, thus eliminating the need for centrifugation at critical junctures. In parallel with work done to optimize the capsule preparation procedure, investigations are made into freeze-drying with liquid N_2 as a coolant as a suitable methods for drying the finished product [28, 29].

In addition to finding and optimizing the chemical process for making the PEM capsules, a large portion of the work involves finding appropriate means of characterization - and tailoring these. For imaging the focus thus far has been on optical microscopy, milling using focused ion beam (FIB) to expose surfaces for imaging with a scanning electron microscope (SEM), as well as scanning tunneling microscopy (STEM). All complimentary techniques. Size and charge determinations will also be done, but more suitable methods for these purposes may yet be found.

Chapter 2

Theory

The following is a theoretical review of some of the most central aspects of the work done in the attempt to create and analyze PEM capsules.

2.1 Tempo-oxidized nanocellulose

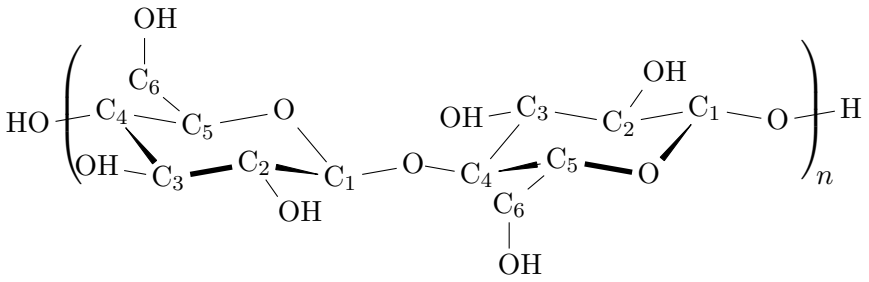

Figure 2.1: Cellulose structure repeat unit with β-1,4-linked D-glucose rings.

The cellulose molecule is as depicted in Figure 2.1. cellulose nanofibrils consist of individual cellulose molecules held together by intra- and intermolecular H-bonds and a network of Van der Waals connections, which are then bundled into microfibrils with the help of hemicellulose and lignin [30]. Tempo-oxidation is a means of separating individual nanocellulose fibrils, mediated by the TEMPO radical (2,2,6,6-tetramethypireperidine-1-oxyl) [22]. The radical oxidizes the OH-group attached to C_6 and it becomes a COO^--group. The TEMPO radical is large, and though it can penetrate into the spongy hemicellulose, only OH-groups exposed at the surface of the nanofibril will be oxidized. From Figure 2.1 it becomes clear that alternating OH-group will be oxidized [22]. After mechanical treatment,

individual negatively charges nanocellulose fibrils with a diameter of $\sim 3\mathrm{nm}$ are released as a result of delamination [14, 31].

2.2 Multilayer microcapsules

Polyelectric multilayered (PEM) capsules can be assembled through three major strategies: electrostatic assembly of oppositely charged polyelectrolytes, hydrogen bonding and covalent bonding [15]. The assembly is done in a layer-by-layer (LbL) fashion under controlled pH, polymer and core-template concentration, and ionic strength of the solution. Although the process is generally stepwise, attempts have been made to use a continuous process [32]. Some of the advantages of a continuous process is the possibility of limiting material consumption, which is one of the main drawbacks thus far with batch processes, in addition to being time consuming [15].

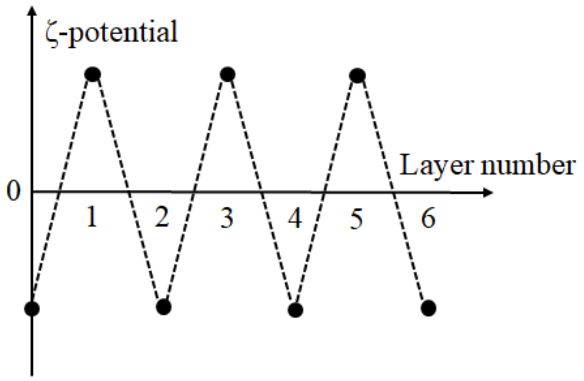

Figure 2.2: Illustration of the general charge reversal (ζ-potential) seen when subsequent polyelectrolyte layers are added to a PEM capsule. Adapted from [25].

When using oppositely charged polymers to assemble microcapsules, the main driving force for assembly is electrostatic force. This was first done by Sukhorukov et al., using a stepwise process with centrifugation steps to remove excess polymer material [25, 26]. For each layer that is added the surface charge will be reversed [25, 33], enabling the next layer to be adsorbed as well as aiding in the prevention of agglomeration through electrostatic stabilization [34]. The charge reversal i illustrated in Figure 2.2, where the ζ-potential is shown to alternate for each subsequent layer. When working with excess concentrations, washing steps become necessary to remove unadsorbed polymer material. This is done using centrifugation. The consequence of not performing washing steps would be that the polymer meant to create the next layer would, when added, adsorb to the oppo-

sitely charged polymer in solution, as apposed to adsorbing at the capsule surface [35].

Of the many factors controlling the growth of the layers, one of the most significant seems to be the ionic strength (i.e. salt concentration) [36]. Other important parameters include charge density [37], as well as interaction time [37–40]. While the way these parameters affect the layer thickness will of course depend on the chosen polymers, the general trend shows that a high salinity gives thicker layers and that it is the highest salt concentration (rather than the last) which determines the final thickness [36–41]. It has also been observed that matching the charge density between the adsorbing polymer and the charged surface yields the thinnest layers [37]. The layer thickness vs. interaction time curves will in most cases follow an approximate S-shape, such that once a certain amount of time has passed the thickness has reached a maximum and the graph flattens [37–40].

The template may be almost any charged particle [42], but latex, and precipitated $CaCO_3$ (PCC) have been used extensively [17, 25, 26, 43]. Although spherical templates are by far the most common, the process has successfully been carried out also using elliptical and even square templates [17]. Interestingly, is has been shown that the porosity may influence the adsorption behavior [44].

2.3 Rheology

Rheology is the study of how matter deforms and flows. For fluids, flow is best described by viscosity (η), which connects the shear stress and strain rate (a permutation of Newton's law),

$$\tau = \eta\gamma \tag{2.1}$$

In equation 2.1, τ denots the shear stress while γ is the strain rate (also known as shear rate). The shear stress is determined by $\mathbf{F}/A$, where the force ($\mathbf{F}$) is parallel to the area (A) upon which the force acts. Expressed as s^{-1}, the strain rate is the rate of deformation. At low strain rates polymer suspensions display a linear relationship between shear stress and strain rate, but as the the strain rate is increased deviations generally occur. Suspensions following a linear slope are termed Newtonian. The two types of deviations from Newtonian behavior are shear thinning and shear thickening. In these cases viscosity is dependant on the strain rate, and apparent viscosity is defined,

$$\tau = \eta(\gamma)\gamma \tag{2.2}$$

The apparent viscosity at a given strain rate is the slope of the line drawn between

the point and the origin [45]. For polymers, shear thinning is most commonly seen. The implication of this is that viscosity decreases as the shear rate increases. This behavior is illustrated in Figure 2.3. For many polymers a linear proportionality is seen at low shear rates. From this linear section, a zero shear rate viscosity can be extrapolated.

Viscosity is a measure of friction between molecules and is dependent upon a number of factors, including intermolecular forces and free volume [46]. For polymers these interactions are dependent on a number of factor connected to the extension of the polymers in solutions [47]. Of note are molecular weight, chain flexibility, solvent quality, concentration and entanglement [45, 46, 48]. Crystallinity of polymers chains in consort can also be of consequence [46].

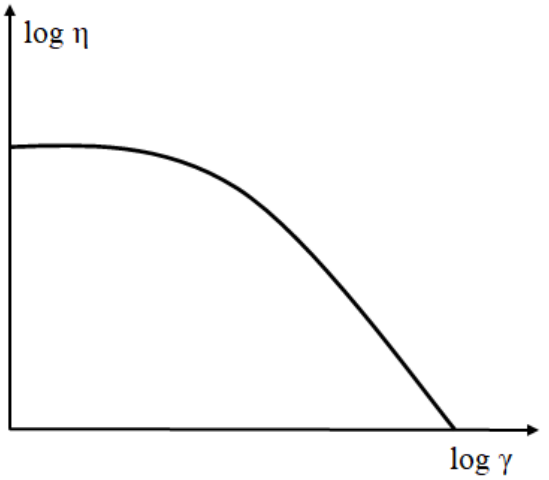

Figure 2.3: Illustration of the shear thinning behavior observed in polymers. Adapted from [46].

Polymer suspensions are complex and cannot by descried by simply viscous or elastic models, the behavior is modeled more comprehensively using viscoelasticity. The viscoelastic behavior of is most usefully investigated by oscillating measurements [45, 46]. The stress and strain behavior becomes time dependent. If the system were elastic and a stress was applied sinusoidally, the shear stress would be greatest at the extreme points of the oscillation and zero when the deformation was zero [45]. This means that the strain is in phase with the applied stress [46]. However, if the system were viscous the shear stress would be largest as the shear rate was largest, and would be zero at zero shear rate. In other words the shear stress would be largest at zero deformation [45]. In this case the strain is out of phase with the applied stress by a phase angle (δ) of $90°$.

A viscoelastic system would display a phase angle (δ) somewhere between $0°$ and $90°$. The exact angle is related to energy dissipation relative to energy storage - the viscous and elastic behavioral components respectively [46]. In essence there is a lag between the applied stress and the strain response. The system can as such be characterized by a combination of the in-phase and out-of-phase components of the stress as a function of strain [45, 46]. The viscosity in equation 2.1 is replaced by the shear storage modulus (G') and the loss modulus (G''),

$$G' = G_0 \cos \delta \tag{2.3}$$

$$G'' = G_0 \sin \delta \tag{2.4}$$

2.3.1 Measurements

Viscosity may be measured by directly measuring the time of flow with applied force. This is the case for a capillary viscometer, where the time it takes for the liquid level to drop from one point to another under influence of gravity is measured. The main disadvantage of capillary viscometers is the inability to vary the shear rate [47].

In other cases rotational forces are applied to the liquid. This is the case for concentric-cylinder and cone-and-plate viscometers. These viscometers have the added capability of varying the rotation speed and thus the shear rate. The two mentioned viscometers are mainly differentiated by geometry of the rotating components. The concentric-cylinder viscometer consists of to concentric cylinders, where one cylinder is rotating [47]. Generally this would be a cup to hold liquid, and a bob to lower into the cup. The liquid will exhibit resistance to the rotation which will be transmitted through the liquid and produce a measurable torque on a non-rotating cylinder [47]. The shear rate can be varied both by changing the rotational speed or by changing the gap between the cup and bob [47]. If the geometry is kept constant and the angular velocity is changed, the viscosity of different fluids can be compared. If the outer cylinder were to rotated the laminar flow would be stable, while a rotating bob produces centrifugal force inducing a more turbulent flow. However, commercial instruments generally rotate the inner cylinder, as this provides greater versatility [47]. Cone-and-plate viscometers are based on the same principles, though other mathematical formulas apply. In this case a rotating cone touches a plate at its apex, and the fluid is placed between the two before the cone is lowered [47]. To measure non-Newtonian behavior, both geometries are widely used.

2.3.2 CNF suspensions

The rheological behavior of CNF suspensions is complicated even further than described up to this point. Each fibril consists of multiple molecules, forming a predictable structure [30]. Thus it is not the interaction between separate molecules that is of consequence, but the interaction between nanofibrils. The fibrils consist of both crystalline and disordered domains [48], lending stiffness and flexibility to the fibrils respectively. This more complicated molecular structure gives rise to some interesting properties.

For viscosity as a function of shear rate, the viscosity is commonly seen to decrease as the shear rate increases. The relationship can be expressed by

$$\eta = k\gamma^{-n} \tag{2.5}$$

where k is the flow index and n is the power-law exponent. If the fluid behaved in such a way that the exponent was zero, it would be a Newtonian fluid [48]. When the viscosity is reported as a function of concentration (c), another power law emerges:

$$\eta = c^n \tag{2.6}$$

In this case the exponent (n) is empirically determined. The concentration in equation 2.6 is most correctly specified as volume concentration, in accordance with Einstein's initial theory on viscosity. This theory was based on the behavior of colloidal particles in liquid [47].

When viewing plots of viscosity as a function of shear rate, a shear thickening effect becomes apparent at low shear rates upon decreasing the shear rate [31]. This carries the ramification that a zero shear rate viscosity cannot be extrapolated from measured data, and implies that shear history may play a role in the expressed viscosity. Additionally, when increasing and decreasing shear rate, hysteresis is observed [31].

When considering the properties of CNF suspension several other factor may need to be taken into consideration. One is the propensity for fibrils to form clusters when they collide [48]. Other include surface roughness in combination with the lubrication effect, wall depletion effects and shear banding [48].

2.4 Zeta Potential

Particles in solution can acquire charge. This is true for any submerged surface, but the focus here will be on particles. Two of the main charing mechanisms are preferential adsorption or desorption of ions at the surface and ionization or dissociation of a surface group [47]. Charge is not purely a surface phenomenon. If a surface is charged, a layer of opposite charge (i.e. countering the charge at the surface) will accumulate around the particle and extend into solution. This layer is known as the electric double layer. The electric double layer is diffuse, having no discrete endpoint. The amount of accumulated charges has a taper such that as the distance from the surface approaches infinity, the amount of accumulated charge approaches zero [47]. How quickly the charge tapers off is often termed the thickness of the double layer (κ^{-1}). The valence and concentration of electrolytes in solution will play a large role in determining the extension of the double layer. The extension decreases with increasing valence and concentration, and the potential drops more dramatically within a shorter distance from the surface. This potential (ψ) drop is determined by,

$$\psi \; = \; \psi_0 \exp -\kappa x \tag{2.7}$$

where ψ_0 is the potential at the charged surface, and x is the distance from the surface. For spherical particles the same basic equation holds, but linear terms are replaced by radial terms. The potential drop is equal around the entire particle, when R_s it the radius of the particle and r is the distance from the particle center,

$$\psi \; = \; \psi_0 (^{R_s}/_r) \exp -\kappa (r \; - \; R_s) \tag{2.8}$$

If two double layers come very close they will begin to interact. The potential between the two charged objects starts to overlap and a repulsion is created. In addition to the electrostatic repulsion force, osmotic pressure is generated. In the area between the two surfaces the electrolyte has a higher concentration, which creates the osmotic pressure. Note that the repulsive forces between two surfaces decreases with increasing electrolyte concentration (if compared at the came separation) [47].

A further distinction within the electrical double layer is between ions which are considered adsorbed at the surface, and those that extend into solution. In a capacitor model, all opposite charge would be accumulated at the charged surface, but crowding prohibits this [47]. A saturation limit is approached near the surface. The ions which are considered adsorbed are known as the Stern layer, extending a distance (δ) from the charged surface [47]. As the electrolyte concentration in-

creases, and increasing amount of the potential drop will happen within the Stern layer. At the distance δ from the charged surface, the surface of shear is found.

The surface of shear is the boundary within which the ions are considered to move together with the particle in solution. The potential at the surface of shear is known as the zeta (ζ) potential. When the electrolyte solution is dilute, the magnitude of the ζ potential can be considered to coincide with the charge at the particle surface. Even when this is not the case, ζ potential is none the less considered interesting [47]. The ζ potential is commonly measured by quantifying the movement of particles in an electric field. The mobility (u) of the charged particles is given by:

$$u = \frac{2\epsilon\zeta}{3\eta} \tag{2.9}$$

The mobility is not only a function of the ζ potential, but also depends on the permittivity (ϵ) and viscosity (η) of the medium. The ζ potential is considered an important parameter of colloidal (or semi-colloidal systems), as it can be considered a good measure of stability. All other factor being equal, the system with with the largest ζ potential will be the most stable [47]. Stability is here a term used to describe resistance to agglomeration/coagulation/flocculation.

2.5 Particle size

Size measurement may be done in many ways, including filtering with progressively smaller filters, sedimentation measurements, gas adsorption studies, area calculations from microscopy images and laser diffraction measurements. Spherical geometery is often assumed or approximated, since the size of a sphere can be accurately determined from a single number [49]. When a particular method is used, it is important to be aware that the measured size will vary based on the which particle parameter is the basis for the measurement. If the diameter can be measured directly, this provides a mean diameter known as D[1,0]. The diameter for each particle is measured and divided by the number of particles [49]. This is probably the most intuitive way of measuring size. If however the projected area of the particle is measured, the average diameter would be dependent on the square root of the diameter squared. The diameter (d) of a circle as a function of area (A) is known,

$$A = \pi \left(\frac{d}{2}\right)^2 \tag{2.10}$$

$$d^2 = \frac{2A}{\pi} \tag{2.11}$$

From the equations 2.10 and 2.11 it can be determined that the mean diameter would be given by:

$$\sqrt{\frac{d_1^2 + d_2^2 + \ldots + d_n^2}{n}} = \sqrt{\frac{\Sigma\, d^2}{n}} \tag{2.12}$$

The same mean diameter calculations from equation 2.12 would apply when measurements of the particles' surface were used. Remember that the surface area of a sphere is given by $4\pi r^2$. This mean diameter is known as D[2,0], since the denominator is a squared term. This line of reasoning can be extended to volume measurements, giving a mean diameter with a cubed denominator known as D[3,0]. The zero in the naming refers to the numerator being directly dependent on the number of measured particles.

Moment mean diameters eliminate the need for counting large amounts of particles. For moment means diameters at one power are added together in the denominator, and diameters at another lower power are added together in the numerator [49]. Two such means are the surface area moment mean (D[3,2]) and the volume or mass moment mean diameter (D[4,3]), where the D[3,2] has d^3 dependence and the D[4,3] has a d^4 dependence,

$$D[3,2] = \frac{\Sigma\, d^3}{\Sigma\, d^2} \tag{2.13}$$

$$D[4,3] = \frac{\Sigma\, d^4}{\Sigma\, d^3} \tag{2.14}$$

The moment means indicate the central point around which distribution will rotate. This could also be termed the center of gravity of the distribution, with respect to either surface area or volume/mass [49]. Being aware of which mean diameter is being used at any one time becomes important when diameters are to be compared. If the mean diameter is calculated in different ways, the outcome will be different and direct comparisons are not correct. An additional factor to be aware of when evaluating distributions is that the mean may not always be at a diameter that particles physically assume. This is mainly true for bimodal distribution, where the mean will fall somewhere between the two maxima. The diameters may yet be compared, but other measurements such as the mode or median may better represent the actual particle sizes [49].

2.6 Centrifugation

When discussing diffusion it is natural to start with a discussion of sedimentation. The forces operating on a particle will be dependent on its volume (V) and density (ρ_2) (i.e. the mass), as well as the density of the surrounding medium (ρ_1). Both gravity and friction will play an important role. The force due to gravity ($\mathbf{F_g}$) and buoyancy ($\mathbf{F_b}$) act against each other, giving a net acceleration,

$$\mathbf{F} = \mathbf{F_g} - \mathbf{F_b} = V(\rho_2 - \rho_1)\mathbf{g} \tag{2.15}$$

If the particle is moving in one direction, the fluid resists the movement by an oppositely directed force [47]. This gives rise to Stokes' law, which determines the friction force ($\mathbf{F_f}$) acting on the particle,

$$\mathbf{F_f} = \pi\eta R_s\mathbf{v} \tag{2.16}$$

where R_s is the particle radius and **v** is the velocity. When the forces from equation 2.15 and 2.16 are balanced and the volume (V) is substituted with $4/3\pi R_s^3$, the following equations for velocity ($\mathbf{v}$) and particle radius (R_s) emerge:

$$\mathbf{v} = \frac{2}{9}\frac{R_s^2(\rho_2 - \rho_1)\mathbf{g}}{\eta} \tag{2.17}$$

$$R_s = \left(\frac{9\eta v}{2(\rho_2 - \rho_1)g}\right)^{\frac{1}{2}} \tag{2.18}$$

As $v = \frac{\Delta x}{\Delta t}$, it becomes it becomes simple to work out the sedimentation time from equation 2.17,

$$\Delta t = \Delta x\frac{9\eta}{2R_s^2(\rho_2 - \rho_1)\mathbf{g}} \tag{2.19}$$

To relate equation 2.19 more specifically to centrifugation the gravitational force must be substituted for the forces acting in the centrifuge. The simplest way to accomplish this is to use the relative centrifugal force (*RCF*) . This is specific to the given centrifuge, since it otherwise would be necessary to take into account the distance from the center of rotation to the position of the particle before and after centrifugation using the sedimentation coefficient,

$$s = \frac{\ln(r_2/r_1)}{\omega^2(t_2 - t_1)} \tag{2.20}$$

which is equal to the sedimentation velocity per unit of centrifugal acceleration [47]. The angular velocity is denoted by ω, while the particles are at position r_1 at time t_1 and position r_2 at time t_2. The RCF can be related to the angular velocity by the proportionality between the centrifugal force ($\mathbf{F_c}$) and the gravitational force,

$$RCF = \frac{\mathbf{F_c}}{\mathbf{F_g}} = \frac{m\omega r}{m\mathbf{g}} = \frac{\omega r}{\mathbf{g}} \tag{2.21}$$

The effect of the difference in distance during centrifugation on the centrifugal force is generally neglected. Then the forces acting on the particles in the centrifuge are $RCF \cdot \mathbf{g}$, and equation 2.19 can be used to determine the time needed to remove particles of desired minimum radius from the supernatant.

2.7 Optical Microscopy

Optical microscopy utilizes visible light to create an image. The light travels through a system of lenses, before a parallel beam is focused into a point by a final convex lens, known as a the objective lens. The point at which the beam is focused is at a distance *f* from the lens, termed the focal length [50]. Focusing light to an sharp point requires monochromatic light, while white light is a combination of many wavelengths. The implication of this being that the shorter wavelengths are focused at a greater distance from the lens than are the longer wavelengths. This in turn leads to white light being focused into a region of finite size, termed the disc of least confusion [50].

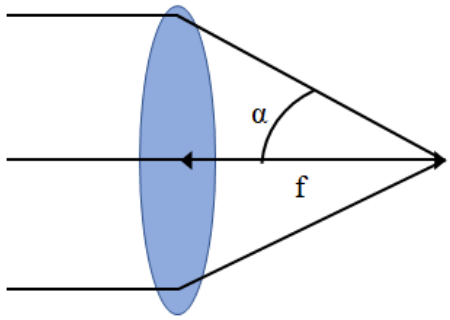

Figure 2.4: The focal length (f) and aperture (α) (half-) angle of an optical lens. Adapted from [50].

The resolution of an optical image it determined by the spacial distribution of intensity from a point source of light, imaged at the focal plane. This mean the intensity will not be contained at one sharp point, but will spread out somewhat.

The with of the peak in light intensity is

$$\delta = 0.61\frac{\lambda}{\sin\alpha} \tag{2.22}$$

where n and α are the refractive index and aperture (half-)angle of the lens respectively, and λ is the wavelength of the incoming light. The denominator ($n\sin\alpha$) is know as the numerical aperture of the lens. The interplay between these various constants, is illustrated in Figure 2.4. In addition to the resolution limit, there is also a detection limit. This is where the signal intensity becomes so low, that it is indistinguishable from the background noise of the system [50].

An additional parameter to be aware of it the depth of field. Since the resolution is finite, it follows that the distance from the lens to an object can be varied slightly without it going out of focus. The distance over which an object remains in focus is the depth of field. The depth of field is given by:

$$d = \delta\tan\alpha = \frac{DOF}{M^2} \tag{2.23}$$

This means that in addition to being related to δ and α, the depth of focus is related to the depth of field (DOF) and the magnification (M) [50]. As the object is magnified to a greater degree, the depth of field becomes smaller.

There are two main forms of images captured using an optical microscope: bright-field and dark-field. To form a bright-field image, the light that transmitted through the sample without scattering is used to form the image. To form a dark-field image, the scattered light is collected to form the image. A possible reason for using dark-field imaging is to detect small or nearly transparent features that scatter light but are virtually drowned out by the intensity of the bright-field image [50].

Near transparent objects may also be imaged with the help of phase contrast or differential interference contrast (DIC). When polarized light passes through a specimen, part of the wave will remain undeviated while part of the wave will be diffracted. The diffracted beam will have a slightly altered phase to the undeviated wave. With phase contrast microscopy both waves are collected and the interference between them gives a resultant wave. Different path lengths create different phase shifts, so the resultant waves of different points give the topographical contrast [50]. For DIC microscopy, only the phase shifted light is collected and the phase shift between points is directly used to provide topographical contrast [50].

2.8 Light Scattering

When particles disrupt a beam of light, information is created that can lead to the particle size [51]. When light hits a particle, it will scatter and the scattering angle is proportional to the particle size [49]. Depending on particle size, Rayleigh or Mie theory is used to give the particle size. For particles smaller than the wavelength of the laser light, Rayleigh equations may be used [51], but for larger size ranges Mie theory offers a comprehensive solution to a complex problem [47, 49]. Mie theory encompasses not only a large size rang, but is applicable to both adsorbing and nonadsorbing particles [47]. There is a distinct advantage to being able to measure sizes over a large range, however there are some disadvantages. To employ Mie theory the refractive index of the material making up the particles and the surrounding medium must be known, as too does the absorption at the given wavelength [47, 52]. Often times the refractive index is known, but the adsorption is guessed or approximated. Though a full mathematical derivation of the Mie theory for particle size analysis is beyond the scope of this work, it is of note that Mie theory is based on the volume fraction of the particles [47, 49, 52]. Boundary conditions are often employed to simplify calculations [52].

The particle size is measured either by studying the variation in intensity of the scattered light with scattering angle, or by comparing the intensity ratios between certain scattering angles [51]. If many particles are struck by the radiation at once, such measurements will give the mean particle diameter. When the measurements are done over time, the sample can be circulated through the beam and give the mean diameter of a larger portion of the sample [49].

2.9 Atomic Force Microscopy

Atomic force microscopy (AFM) lies under the general heading of scanning probe microscopy. The technique uses a cantilever with a probe tip to move across a surface and gauge height. As the tip - placed at the end of a cantilever - moves up and down [53], a laser beam is shown off the cantilever onto a photo diode which measures the tip movement [54]. Van der Waals Forces between the tip and sample determine the deflection [55]. An illustration of the basic working principles can be found in Figure 5.4

There are two main modes of AFM operation: contact or tapping mode. The basics principle of the contact mode is that the tip is in contact with the sample and rasters across the surface so that vertical tip movement may be measured. This is not optimal, and to avoid problems associated with disengaging in valleys, excessive force at the peaks and sample tilt, sample height (Z direction) feedback is used to offset these variations and keep the force exerted by the tip approximately constant [54].

It is a matter of course that dragging a tip across a sample may lead to damage. To avoid damaging sensitive materials, tapping mode is used as a substitute. In this mode the tip is oscillated many times per point at a resonance frequency. The forces exerted by the sample is capable of changing the resonance frequency, so the frequency is kept constant by a piezoelectric motor moving the cantilever in the Z direction [54]. The movement of the cantilever is again translated to a measure of sample height.

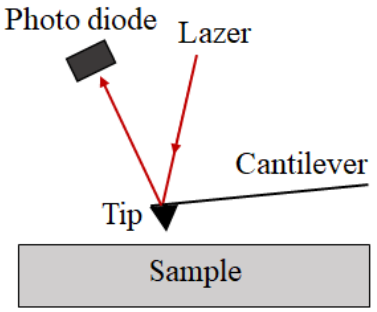

Figure 2.5: Illustration of the basic working principles of an AFM.

The tips lateral extension determines the image resolution to a large degree. Ideally only one atom interacts with the sample, so the tip should be atomically sharp. The tip must however have some lateral extension. As seen in Figure 5.4, the tip has a triangular shape (in 3D this would present as pyramidal). Even if the tip is kept extremely thin, retaining contact with only the apex is not possible when features become steep. Some point along the incline of the tip will also come into contact with the sample and prematurely deflect the tip [54]. The exact nature of the surface measurements and amount of convolution will be dependent on the tip shape. Damaged or unclean tips will exacerbate this issue, and as such it is important to work with new or clean tips [53]. If the tip shape is know the image can be corrected, to some degree [56]. Since only sample height can be measured, undercuts will not be included in the resulting topography. The combination of convolution effects and absence of undercut features, makes diameter measurements of spherical shapes appear tricky. However, a simples solution can be found: by measuring the difference in height between the top of the feature and a point some lateral distance away, the diameter is obtained [57].

2.10 Scanning Electron Microscopy

Scanning electron microscopy (SEM) is a technique whereby electrons are used to create an image. When electrons are accelerated towards a material with a given acceleration voltage (v_{acc}), they will interact with the material by penetrating into it. The geometry and depth of this penetration is termed the interaction volume, and is approximately pear shaped, as seen in Figure 2.6a. The "stem" is at the surface of the material and the volume balloons out below the surface, as a result of collisions with atoms of the sample (i.e. scattering events) [58]. This interaction volume increases with acceleration and energy (i.e. acceleration voltage) and decreases as the atomic number increases. As the acceleration voltage increases so too does the energy, and the electrons penetrate deeper into the sample. If the atomic number increases the interactions become stronger, and the the depth decreases. A more detailed explanation follows below.

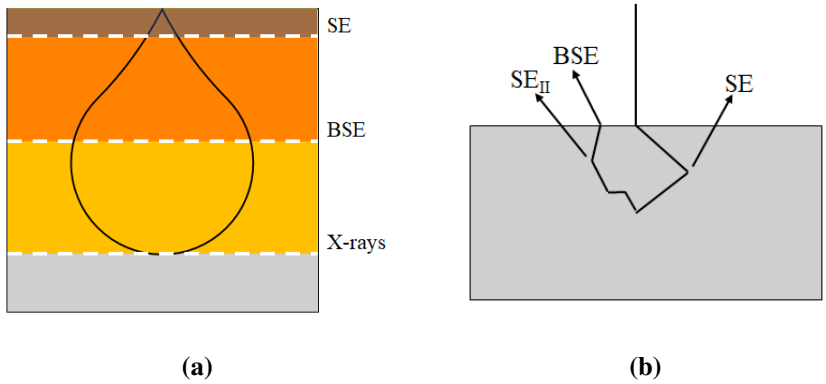

Figure 2.6: Interaction of electrons with the sample in electron microscopy. a) The interaction volume of electrons in the sample (teardrop approximation), and relative escape depths of SE, BSE and X-rays. Adapted from [55]. b) The interaction of incidence electrons with the sample resulting in BSE and SE. Only escaping SEs are depicted.

The "spot size" of the beam is the diameter of the beam/probe (d_p) that interacts with the sample. This property determines the size of the "stem" and thereby the resolution of the image, where a smaller spot size gives better resolution. The spot size is in turn dependent on the current of the electron probe (i_p) - also known as the emission current - and the probes convergence angle (α_p), where the dependence is such that a lower current leads to a smaller spot. The interplay between these properties is illustrated in Figure 2.7. The emission current from the source is dependent on the type of source used. The two most common sources are a tungsten filament and a field emission source, with the field emission source having a

decreased emission current [58]. Thus, a field emission source will necessarily give a smaller probe diameter and better resolution. The difference between the two sources will be elaborated upon below.

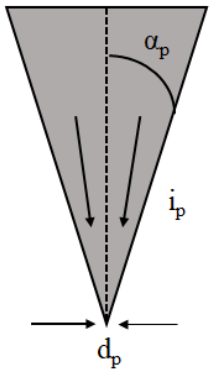

Figure 2.7: Illustration of the spot size given as the probe diameter d_p, determined by the emission current i_p and convergence angle α_p.

SEM usually has a larger depth of field than seen in optical microscopy. The depth of field described as the distance in the z-direction (along the optical axis) that the sample can be moved without the image becoming noticeably blurry, meaning that more than one part of a given structure can be in focus at once. A consequence of this is that the sample can be tilted toward the SE detector for better yield, without a lot of resolution loss. The superior depth of field is a result of the small conversion angle (α_p) of the probe. The result of equation 2.24 is that the depth of field can be increased by increasing the working distance (*WD*) - the distance from objective lens to sample - or reducing the condenser aperture size (D).

$$\alpha \approx \frac{D}{2WD} \tag{2.24}$$

SEMs can be operated in two main ways: viewing backscattered electrons (BSE) or secondary electrons (SE). BSEs are incidence electrons escaping from the sample after mostly elastic scattering events, whereas SEs are electrons freed by the inelastic collision of the incidence electrons within the material. The two types of escaping electrons are illustrated in Figure 2.6b. Generally BSEs mainly contain information about atomic number contrast, because the number of BSEs that escape from the material is proportional to the repulsive power of atomic nuclei. This power is determined by their positive charge (i.e. number of protons), and the number of BSEs becomes higher with increasing atomic number [55]. As the interaction volume becomes larger with lowered atomic number (Z), the elec-

trons penetrate deeper and are less likely to escape. The backscatter coefficient (η) quantifies the number of the number of electrons that escape as a fraction of the primary/incidence electrons [58]. This fraction increases with increasing atomic number, as well as with increasing acceleration voltage [58].

SEs are used to give topographical contrast, because they are only emitted from very close to the surface and are therefore very sensitive to surface incline. The SE yield (δ) is the average number of secondaries escaping as a fraction of the primary/incidence electrons [58]. As the surface feature becomes more parallel with the incidence beam, the number of emitted SEs becomes higher. Sharp changes in the surface, such as corners and points, are accompanied by a large SE emission and show up as a bright spot or line. This is the edge effect, and gives the SEM image a 3D appearance [55]. This effect is illustrated in Figure 2.8a. For case A, the beam is perpendicular to the sample surface, and the region from which SEs can escape is a cylinder of volume $V(0) = (\pi/4)d^2\lambda_{SE}$. In case B the beam is at an angle ϕ to the surface, and the escape region becomes $V(\phi) = \pi(d/2)^2(\lambda_{SE}/\cos\phi)$ [58]. Since the SE yield is proportional to the escape region, it is found that

$$\delta(\phi) = \frac{\delta(0)}{\cos\phi} \tag{2.25}$$

Although SEs are generally used when imaging topography, BSEs also give a significant amount of topographical contrast, since also here more of the interaction volume comes within the escape depth when near an inclined surface. As well as being sensitive to surface incline, SEs can be stopped by features getting in their way, causing a shadowing effect and ultimately leading to an even stronger 3D appearance.

As seen in Figure 2.6b there are more than one type of SEs, classified by how they are generated. $\mathrm{SE_I}$ are generated when the primary electrons first strike the sample, and $\mathrm{SE_{II}}$ are generated when a BSE exits the sample. The implication is that some SEs are generated at a lateral distance from the probe. The SEs generated at distance from the probe can show contrast from structures below the SE escape depth, and play a role in the image resolution. A "skirt" is added to the image resolution function (Figure 2.8b), and contributes to a slight resolution decrease. This decrease is thankfully only minimal, because the large narrow peak generated by $\mathrm{SE_I}$ will dominate.

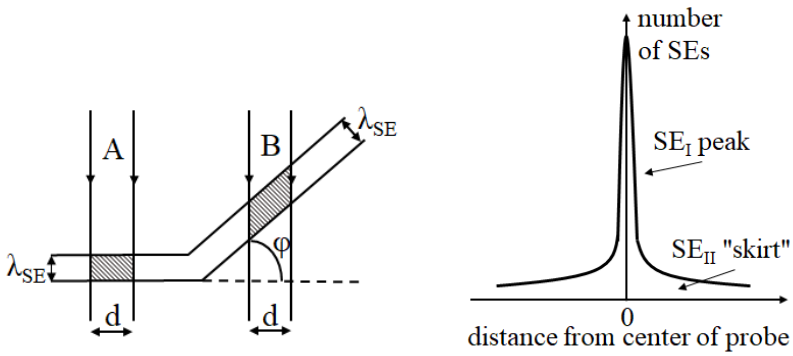

(a) **(b)**

Figure 2.8: (a) The volume form which SEs can escape the sample. The incidence beam is normal to the surface at A, but at an angle ϕ to the surface in B. The volumes are proportional to the shaded areas, that are $\lambda_{SE}d$ for the situation A, and $d\lambda_{SE}/\cos\phi$ for B. (b) The relative contribution of SEs generated in different ways, leading to the total SE resolution function. Note that the SE_{II} generated away from the center of the probe have a small overall contribution, and are only minimally damaging to the resolution. Both adapted from [58].

2.10.1 Optics and Detectors

The electron generation and optics are found in what is known as the column, which is always kept under vacuum. The electrons are generated from a source. As mentioned above the two most common sources are a tungsten filament and a field emission source, with the probe diameter from the field emission source being smaller. A field emission source generates electrons through them tunneling out of the surface potential barrier, while a tungsten filament operates by thermionic emission [58].

The electrons are accelerated by an anode and travel through a system of electromagnetic lenses. The condenser lens system forms the electrons into a coherent beam, and the objective lens focuses the beam by adjusting the lens current [58]. Both lenses play a role in the "spot size". Since the lenses will never be completely symmetrical, a stigmator helps correct for this. For the condenser lens system axial astigmatism arises, wherein the electron beam is slightly elliptical as apposed to the optimal spherical shape. If the beam is elliptical there will be streaking of the image as the focus is changed [58]. The scan lens consists of deflection coils, serving to move the electrons beam and create the scanning motion.

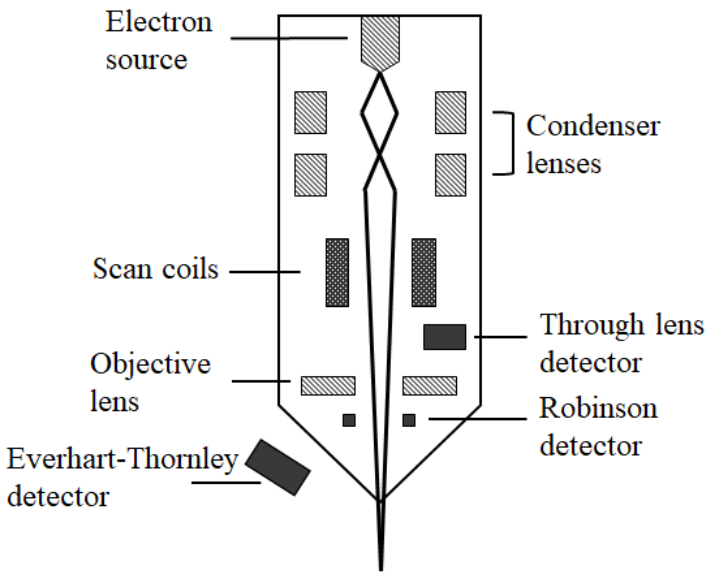

Figure 2.9: Schematic illustration of the SEM electron column with optics and detectors. This is a general configuration that may vary between instruments, with the detector types and setup changing the most. Adapted from [55].

There are three detector depicted in Figure 2.9. The highest up we find the trough lens/in-lens detector (TLD), used in combination with an immersion lens (or projected immersion lens). The specimen sits within the magnetic field of the objective lens, making the working distance effectively zero [59]. The emitted electron spiral within the magnetic field and are collected by the detector mounted above the objective lens [58]. This detector collects all SEs, regardless of direction and thus displays little shadowing. Just below the objective lens we find a Robinson detector, which is usually a solid state device. This type of detector i used to detect BSEs (and is often known simply as a BSE detector). The last detector is the Everhart-Thornley detector (ETD). This detector utilizes a Faraday cage and a scintillator to capture electrons. The electrons must pass through the cage to be detected, meaning that the cage can be positively biased to attract and detect SEs, or negatively biased to drive away SEs and only detect BSEs [58].

2.10.2 Artifacts and challenges

One common artifact when using the SEM is the contamination known as a scan square. When the beam is rastered across the surface material - usually hydrocarbon - is deposited on the sample. Contamination is difficult to avoid, but attempts could be made to work in an ultra clean environment by baking the chamber to

remove contaminants. It is however possible to avoid seeing the effect in images, by capturing images at low and then progressively higher magnifications.

As the magnification is increased the beam is scanned across a smaller area and amount of energy adsorbed at each point increases. As the energy increases so does the temperature, and thermal effects in the form of beam damage may result. These artifacts are alterations to the sample that may easily be mistaken as being innate, and lead to errors in data interpretation. This problem can be overcome by lowering the electron dose. This means for instance scanning across the area faster, though this would lead to poorer image quality. Other solutions are: lowering the spot size, acceleration voltage or magnification, cooling with N_2, and coating the sample (to lead away heat and charge, as well as shield vulnerable structures). However, none of these may be feasible.

A basic challenge faced during imaging is drift. This is particularly noticeable at high magnifications, when the features are small. The entire sample drifts slightly, so using stronger adhesive or letting the sample rest before imaging could mitigate this issue.

With none conducting samples, charging is often seen. This is a build-up of charge on the sample when fewer electrons are being emitted or flowing to ground then are reaching the sample. In a conducting sample, the current flowing to ground (I_s) is the primary beam current (I_p) minus the rate off loss of electrons through emission of SEs and BSEs [58]:

$$I_s = I_p - I_{BSE} - I_{SE} = I_p - \eta I_p - \delta I_p = I_p(1 - \eta - \delta) \tag{2.26}$$

The primary beam current will be constant, while the emission will vary. Charging can often be avoided through coating with a conductive material. A 10-20 nm coating is common [58]. This is greater then the SE escape depth [58]. The SE signal now comes from the coating rather than the sample, but as long as the topography is conserved this poses no problem. The choice of coating material can however be important. Au is a common coating material, but the grain size becomes visible at high magnifications. Pt/Pd coating provide smaller grain sizes and is easy to use for coating. For very high resolution work Cr can be used, but requires the sample to be imaged immediately if oxidation is to be avoided.

A coating is unfortunately not always possible or desired. In such cases appropriate selection of acceleration voltage could be used to do away with the problem. Both η and δ depend on the electron energy (E_0) - which is itself dependent on v_{acc}. At high E_0 there is a low yield of both SEs and BSEs, due to the deep penetration of the primary electrons. This low total yield results in a negative sample charge. As the energy is reduced δ increases and eventually the I_s required to maintain charge

neutrality becomes zero. For very low E_0 the total yield falls dramatically, because the primary electrons do not have enough energy to create SEs and since $\eta < 1$ the sample will again be negative [58]. Between these to points, from here on called E_1 and E_2, the negative charging is absent even for insulating specimens. At these two points the total yield $(\eta + \delta)$ is exactly one and the I_s required to maintain charge neutrality is zero. Between these two points the specimen charge is positive, but SEs attracted back to the sample serve to neutralize this charge. This region is called the zero charging region, and is material specific [58]. The various regions are illustrated in Figure 2.10.

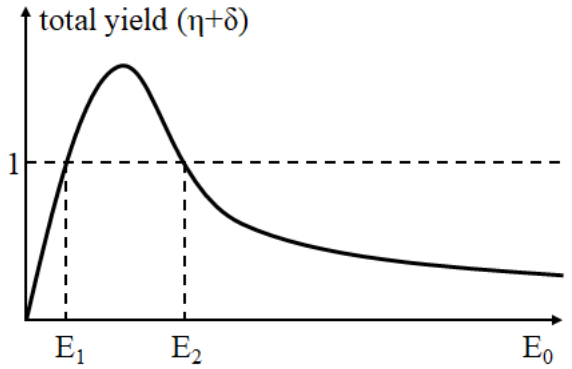

Figure 2.10: The total electron yield curve as a function of the primary electron energy (E_0). In the zero charging region, between E_1 and E_2, charging is no longer a problem for insulating samples. Adapted from [58].

As charging is tied to the number of electrons striking a spot on the sample per time, charging artifacts can also be avoided by varying the beam current, dwell time and magnification [60]. Lowering each of these parameters results in fewer electrons striking the surface per time, reducing the charging.

2.10.3 Energy Dispersive X-Ray Spectroscopy

X-rays have briefly been mentioned. The X-ray emission induced by inelastic collisions between incidence electrons and atoms of the material, can provide elemental information. This technique is known as energy dispersive X-ray spectroscopy (EDX). Excitation is caused when the incident electron has higher energy than the binding energy of the atomic electrons [61]. When the exited atom returns to its ground state, a characteristic X-ray is emitted. This is picked up by detectors and used to identify the element. Peaks in the spectrum will be found mainly at the wavelengths characteristic for the sample atoms. However, if two waves arrive at the detector simultaneously, they will be summed and the peak - called a sum peak

- will appear at higher energy. Additionally, peaks may be difficult to deconvolute if two elements give rise to peaks of similar energy.

At the same time as atoms are excited, the incidence electrons release energy in the form of X-rays. The energy is lost due to deceleration when the incidence electrons experience repulsion from the electron cloud around the atoms of the sample [61]. X-rays along the whole spectrum (up to the energy of the incidence electrons) are produced, and create a background spectrum known as the bremsstrahlung continuum. The final spectrum will consist of both the characteristic peaks and the bremsstrahlung continuum. To do semi-quantitative analysis of the sample composition, the bremsstrahlung continuum is removed prior to analysis.

X-rays can escape from the entire interaction volume of the incident beam [55]. The resolution of the analysis is lowered and elements at different depth will appear in the same spectrum. EDX analysis is therefore not useful for determining if the elements are separate or a compound. The analysis is however quite useful for determining which elements are present where, by scanning an area and creating a map. Non conducting samples to be imaged with SEM are often coated with a conducting layer, and it is important to keep in mind that the elements of this coating will appear in the X-ray spectrum.

2.10.4 Scanning Transmission Electron Microscopy

Scanning transmission electron microscopy (STEM) combines attributes of transmission electron microscopy (TEM) and SEM. STEM images are formed by rastering an electron beam across the sample and collecting transmitted electrons. The contrast is a function of the intensity of transmitted electrons at each point.

TEM image contrast is determined by electron scattering and the path of the transmitted electrons [55]. As electrons pass through the sample they are scattered elastically and inelastically, becoming deviated from the initial straight trajectory of the incident beam. A BF image forms when the scattered beams are blocked, and only unscattered electrons are collected. Areas of the sample that scatter more electrons will appear darker [55]. Factor such as increased thickness, increased mass (i.e. higher atomic number (Z) and density), grain boundaries and dislocations, increasing scattering and create contrast.

DF images are formed when only the scattered electrons are collected. Varying the angle of the detector used to capture DF-STEM images captures electrons scattered at different angles [62]. The same factors effecting the contrast in BF images, are also responsible for the contrast in DF images. However, areas that appear light in the BF images will appear dark, while dark areas will appear light in DF images captured at the appropriate angle [62].

2.11 Focused Ion Beam

The focused ion beam (FIB) is an instrument with many similarities to the SEM. The main difference is that electrons are replaced with ions, typically Ga^+. While the SEM is primarily used for imaging, the FIB additionally has the capacity to use ablation to mill the sample as well as deposition through gas decomposition, both with high precision. The imaging process is termed scanning ion microscopy (SIM). The ion column possesses many similarities to the electron column, with the addition of an aperture. The high energy ions are pulled from the source using an electric field, and then pass through the aperture [63]. The ions are extracted from a liquid-metal ion source (LMIS) [63], consisting of a solid needle surrounded by a reservoir of molten Ga. It is worth noting that the aperture is constantly being degraded by the stream of ions.

The ions are accelerated towards and strike the sample. Upon striking the sample Ga^+-ions, with their significantly larger mass than electrons, will transfer a large amount of energy to the atoms of the sample. The collision may ionize at target atom ejecting them as secondary ions. If the beam is focused on one spot for an extended amount of time, surface material is removed to a such a degree that milling becomes a problem for imaging, but an asset for use in machining.

Imaging is done using SEs emitted upon inelastic collision between the ions and the sample [63]. SIM images have the opposite contrast to SEM images, as well as providing clearer observations of grains contrast (through channeling contrast) [63, 64]. The contrast is a result of the difference in the nature of the collision of an electron and an ion. Monte Carlo (MC) simulations have shown that the interaction volume of ions accelerated at the same energy as electrons, will give rise to a much narrower interaction volume [63].

2.11.1 FIB/SEM

The main reason for combining a FIB and an SEM in the same instrument, is to allow in situ observation of the work done by the FIB. For this purpose the beams are placed at an angle to each other, such that work can be done with the ion beam and observed by the electron beam. To avoid constant realignment of the sample, the sample is placed at eucentric height [64]. This is the horizontal center of the objective lens, and the coincidence point of the two beams [64]. The sample can then be tilted around it's axis, without movement of the image.

Essential parts of the work done with the FIB are ion milling and material deposition. To correctly position markers, monitor processes and designate correct areas for work SIM images are used [63, 64]. Ion milling (also known as sputtering) is the result of elastic collisions between the heavy ions and the sample [63]. Such

collisions result in the removal of surface atoms. The amount of surface material removed as a function of time, can be approximated by multiplying the sputtering yield and the beam current [64]. The yield is the average number of atoms removed as a fraction of incidence ions [64], while the beam current quantifies the number of ions reaching the sample per unit time. The sputter yield is material dependent, and is given is for an ion beam of $30\,\mathrm{kV}$ acceleration voltage at $0°$ tilt as a function of atomic number in Figure 2.11. Milling rates will also depend on the crystal orientation, but this has not been accounted for in Figure 2.11.

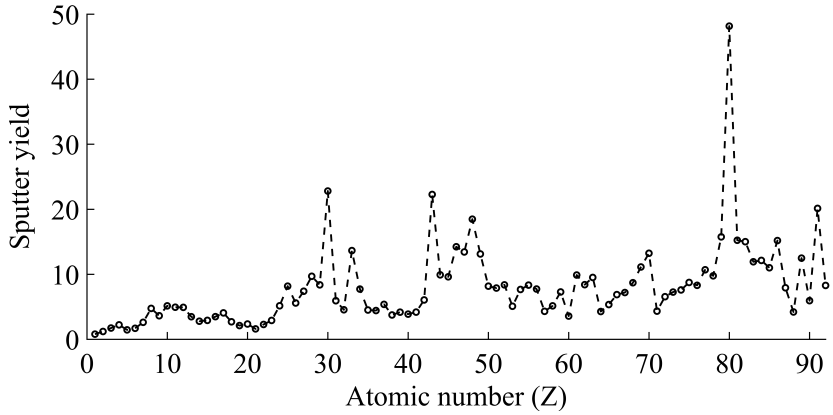

Figure 2.11: The sputter yield (i.e. the number of atoms removed as a fraction of incidence ions) as a function of atomic number, when using $30\,\mathrm{kV}$ Ga^+ ions. The beam is perpendicular to the sample surface. Data from [64].

To ensure the ions cut completely through the desired sample and that the face is of good quality, the dwell time and current of the beam must be appropriately selected [63]. This ensures the correct ion dose. A wide range of currents are available, but the one that gives an acceptable amount of damage will be highly material dependent.

For deposition of thinfilms or markers, a precursor gas diffuses to the surface and is decomposed by the ion beam (or in some cases the electron beam). The precursor selection is crucial. The gas must have sufficient sticking probability to stick to the surface is in large enough quantities and must - upon ion bombardment - decompose at a faster rate than the deposited material is sputtered away [64]. If dwell time, refresh time and ion current are not optimized, the deposition rate will be slowed - or even become negative (e.i. sputtering occurs). The optimum dwell time would be of sufficient length to decompose the maximum amount of precursor, but short enough to remove a minimal amount of deposited material [64].

2.11.2 Artifacts and challenges

There are a substantial number of challenges when using a FIB. Therefore this text will outline each one briefly. First, as noted, there is a large amount of energy transfer between the incoming ions and the surface atoms. This can lead to the sample heating up and charging. Thermally stabilizing the sample is necessary to prevent drift during milling and deposition [64]. A large amount of charging can lead to structural damage, and it is in the users interest to avoid this by grounding and coating the sample to suppress charging.

While milling a sample there are three main complications that may arise. Ion implantation from the source can cause damage to the imaging surface and change its characteristics [64]. This can be avoided by changing the acceleration voltage. Striations (also known as curtaining) occur when materials of different hardness or thicknesses are sputtered. Depositing what is known as a planarizing layer of Pt can aid in stopping curtaining [64]. Redeposition of milled material is also a major problem. This can be redeposition on an imaging surface or redeposition in a high aspect ratio trench limiting the possible depth or in a void creating erroneous contrasts. Reducing the milling rate and/or changing the dimensions of the area to be milled can help [64]. Finally, all the energy of the beam will not be concentrated in a precise spot. There will always be a beam tail of lower intensity, giving some milling in a tapered angle beyond the designated boundaries [63]. This effect can be avoid by tilting the sample into the beam while it is being milled [63], or milting the sample with successively lowered beam currents. The latter of which can also be of help in minimizing redeposition.

For deposition it is pertinent to remember that the deposited material is likely to display non optimal material properties. There will always be some incomplete redeposition leading to incorporated impurities. These impurities will give the material some altered properties [64]. Additionally, if the deposition parameters are suboptimal, sample atoms may be sputtered away. This can be limited by applying a thin layer at a low current, before employing a higher current to deposit the remainder of the desired thickness. The thin layer will act as a barrier toward sputtering.

SIM images are created using the ion beam, so many of the same challenges will present themselves. Most notably the imaging an milling will happen simultaneously. So changes to the sample may happen while imaging. Other effects that pertain to this are ion implantation and, with certain materials, grain growth in the sample.

Chapter 3

Materials and Methods

Deionized (DI) water was used for all solutions and suspensions. Consequently sample preparation for optical imaging and washing was also done with DI water. Gloves were worn at all times when handling samples and reactants, both to comply with HSE regulations and to reduce sample contamination.

3.1 Fabrication of $CaCO_3$ template particles

Materials. Na_2CO_3 and $CaCl_2 \cdot H_2O$ powders from VWR were used.

Method. Homogeneous spherical $CaCO_3$ particles were obtained by mixing $0.33\,\mathrm{M}$ solutions of Na_2CO_3 and $CaCl_2 \cdot H_2O$ [65]. Once combined, the mixture was stirred rigorously for $30\,\mathrm{s}$, before washing [66]. Washing was done by three rounds of centrifugation. The particles were subjected to centrifugation for $3\,\mathrm{min}$ at $1700\,\mathrm{rpm}$. Then the supernatant was removed and the solution was re-diluted. Gentle shaking and $2\,\mathrm{min}$ of sonication in an ultrasound bath was used to redisperse the particles, before the next centrifugation step. After the final round of centrifugation, the solution was only diluted to approximately $25\,\mathrm{mL}$. Freeze-drying of the particles was done using a *Biobase Biodustry BK-FD12S* with freezing at -80 °C and drying at $30\,\mathrm{Pa}$.

Analysis. Bright field images were taken using a *Leica Leitz DMRXE* optical microscope and analyzed using ImageJ's particle analysis tool, to find the average particle size. The image was transformed to an 8-bit greyscale image and the light background was removed. Then the brightness/contrast was adjusted and a threshold was set using default setting to create a black and white image with the desired particle outlines. Particle analysis was done with a minimum spherical

area of $1\,\mu m^2$ and maximal area of $100\,\mu m^2$, so as to remove small specks on the image that were clearly not particles and the multiple particles in close proximity interpreted as one larger particle by the software. Circularity was designated to be between 0.8 and 1, to remove most of the agglomerates and exclude particles partially outside the image. Particles on the edge were therefore not explicitly excluded from the estimate. A histogram of diameters was used to further weed out the outlier (i.e. very small and very large particles). In total approximately 1300 particles were included in the analysis.

As a comparison a *Malvern Mastersizer Hydro SV* provided volume and number distributions of particle diameter, leading to the volume moment mean diameter (D[4,3]). After a baseline was established, the sample was added to the measurement cell. The cell was cleaned with isopropanol between measurements.

3.2 Microcapsules

The process used is an adaptation of that used by Sukhorukov et al. [25–27].

Materials. The template particles were spherical $CaCO_3$ (PCC) particles, fabricated as described previously. PDADMAC (polydiallyldemethylammonium chloride) from Sigma Aldrich of molecular weight 200-350 kDa was chosen as the cationic polymer. TEMPO-oxidized CNF homogenized with 2 passes at 1000 bar, formed the outer layer of the PEM microcapsules. The CNF-T is known to have a negative charge of $910\,\mu mol \cdot g^{-1}$ [67], and was found to have a dry weight percentage of 0.85% (assumed to be the total solid content).

Method. The basic steps of the process:

1. Make separate solutions/suspensions of PDADMAC,PCC and CNF-T.
2. Mix PCC suspension with equal volume of PDADMAC solution, let interact.
3. Washing: centrifugation 3 times, with sonication between each step.
4. Add the precipitate to CNF-T suspension drop-wise, let interact.

A suspension of 0.1% (w/w) PCC was used and PDADMAC was diluted to $1\,mg \cdot mL^{-1}$ with 10 mM NaCl [33, 41, 68, 69]. Before mixing PCC agglomerates were dispersed. This was accomplished through 5 min of sonication in an ultrasound bath. The PCC was allowed to interact with PDADMAC for 30 min [37–40], while stirring at $\simeq$130 rpm. Washing was done using a *Heraeus Labofuge* or an *Eppendorf Centrifuge 5810* at 1700 rpm for 3 min, to remove unadhered - i.e. excess - polymer. This rotation speed is equated to a force of 562 RCF. The centrifugation time was calculated using equation 2.19, in order to precipitate particles with the minimum size of $0.5\,\mu m$. This overestimation was done due to the heterogeneity of

the PCC and due to the *Heraeus Labofuge* having a long acceleration time, leading to uncertainty in the time spent at the desired rotation speed. Between each centrifugation step the supernatant was removed and the suspension was re-diluted to original volume. Gentle shaking (i.e. manually tapping the centrifugation tube against a hand) and $2\,\mathrm{min}$ sonication in an ultrasound bath was used to redisperse the capsules and reduce - hopefully even prevent - agglomeration [25, 26]. After the final washing step, the suspension was re-diluted using only $20\,\mathrm{mL}$ of DI water.

Once the single layer capsules (the term used to describe the product after PCC and PDADMAC interact) were completed, they were allowed to interact for $30\,\mathrm{min}$ with a suspension of CNF-T, dispersed by shaking as well as stirring at $\simeq 800\,\mathrm{rpm}$ for minimum $1\,\mathrm{h}$ [37–40]. The single layer capsules were added drop-wise [70], while stirring the CNF-T suspension at $\simeq 130\,\mathrm{rpm}$. The amount of CNF-T needed to cover the surface was estimated to be $15\,\mathrm{mg/g}$ $CaCO_3$. To this end it was assumed spherical particles, average template particle diameter of $5\,\mu\mathrm{m}$, a fiber diameter of $5\,\mathrm{nm}$ and length of $1\,\mu\mathrm{m}$ [67]. The density of $CaCO_3$ and CNF-T are known to be $2.71\,\mathrm{g}\cdot\mathrm{cm}^{-3}$ and $1.55\,\mathrm{g}\cdot\mathrm{cm}^{-3}$ respectively [71]. The calculated amount was doubled to account for larger particles, smaller fibers, porosity and uncertainties surrounding the conformation of polymers attaching to the particle surface. The CNF-T concentration was varied from $0.015\,\mathrm{mg}\cdot\mathrm{mL}^{-1}$, to $0.0015\,\mathrm{mg}\cdot\mathrm{mL}^{-1}$ and $0.000\,75\,\mathrm{mg}\cdot\mathrm{mL}^{-1}$, though the same relationship between amounts of PCC and CNF-T was maintained each time. Henceforth the term microcapsules will be used to describe the product after single layer capsules have interacted with CNF-T. Freeze-drying of the microcapsules was done using a *Biobase Biodustry BK-FD12S*, with rapid freezing in liquid N_2 and subsequent drying at $30\,\mathrm{Pa}$ [28, 29]. The freeze-drying procedure described by Torstensen et al. (2018) was used with some modifications [28]. A small Cu sample holder containing a few drops of solution was immersed in liquid N_2, before being placed in a smaller liquid N_2 bath in the freeze-dryer. A small Si wafer was stuck to the bottom of the sample holder before the sample was added, using double sided tape.

Analysis. The CNF-T fibril diameter was investigated using a *Veeco Metrology AFM diMultimode V*, in tapping mode (ScanAsyst Air) under ambient air conditions [72]. Measurements were performed using a dilute sample at 0.001% (w/w), dried on mica at either $70\,^{\circ}\mathrm{C}$ or $90\,^{\circ}\mathrm{C}$. For each sample 80-110 fibrils where measured. Height profiles were extracted using Gwyddion, following row alignment of the images. The median of difference method was chosen for the alignment. After hight data was extracted, some images were adjusted for visual effect. Extreme heights were excluded, by limiting by limiting the range. A *Rheometer Physica MCR 301* was employed for rheological experiments, operated with cup-and-bob geometry (cup height $68\,\mathrm{mm}$ and diameter $28.9\,\mathrm{mm}$, and bob height $40\,\mathrm{mm}$ and

diameter $26.7\,\mathrm{mm}$) at $20\,^{\circ}\mathrm{C}$. Suspension were prepared from the same 0.5% (w/w) stock solution. Dispersion of the stock solution was achieved through stirring using an *IKA Eurostar digital* at $1500\,\mathrm{rpm}$ for $10\,\mathrm{min}$, while the dilute suspensions were homogenized by stirring at $1000\,\mathrm{rpm}$ for $3\,\mathrm{min}$. The rheometer was allowed to equilibrate for $1\,\mathrm{h}$ before measurements were performed, and each sample was given $2\,\mathrm{min}$ to rest an stabilize at the measurement temperature. Sweeps from high ($1000\,\mathrm{s}^{-1}$) to low ($0.1\,\mathrm{s}^{-1}$) and low to high shear rate were run, before 10 measurements at shear rates of $1\,\mathrm{s}^{-1}$, $10\,\mathrm{s}^{-1}$ and $100\,\mathrm{s}^{-1}$ respectively. One minute of rest time was given between the different measurement categories.

The ζ-potential of the single layer capsules was investigated using a *Malvern Zetasizer Nano ZS* in combination with folded capillary cells [25, 26, 70, 73, 74]. The temperature was set to $20\,^{\circ}\mathrm{C}$ for all measurements. The single layer capsules were also attempted sized using the *Malvern Mastersizer Hydro SV*. The same procedure was used as for $CaCO_3$ template particle measurements.

After interaction with CNF-T the resulting structures were mainly analyzed visually using a FIB/SEM (*FEI Helios NanoLab DualBeam*), a *Hitachi S-5500 S(T)EM*, as well as a *Carl Zeiss Axio Scope.A1* optical microscope. A detailed procedure for the FIB/SEM operation will follow. The STEM was operated in transmission mode, using samples deposited on holey carbon film TEM-grids and detector angle varying from 0-55°. Samples for use with the optical microscope were simply deposited between a glass slide and glass cover slide. BF, DF images were captured, additionally DIC and phase contrast were utilized.

Troubleshooting. The effects of adding single layer capsules to a CNF-T suspension was thoroughly investigated. The presence of excess Ca^{2+}-ions was investigated by combining equal volumes of supernatant (after three and four wash cycles respectively) and $0.3\,\mathrm{M}$ Na_2CO_3, while monitoring for $CaCO_3$ precipitation. The effect of remaining PDADMAC in solution was explored by combining $5\,\mathrm{mL}$ supernatant (after three and four wash cycles respectively) with $25\,\mathrm{mL}$ of $0.015\,\mathrm{mg}\cdot\mathrm{mL}^{-1}$ CNF-T. The supernatant was added drop-wise. The solutions were allowed to interact for 30-60 min with $\simeq 130\,\mathrm{rpm}$ stirring. Care was taken to replicate as closely as possible the conditions when adding single capsules to CNF-T suspensions.

3.3 FIB/SEM

FIB/SEM as a characterization technique is discussed separately, due to the many variables that must be controlled.

Sample preparation. Si wafers were cleaned using O_2 gas in a *Diener Electronics Femto* plasma cleaner, at 50% power for $42\,\mathrm{s}$, lending some hydrophilicity for

better sample deposition. The microcapsule solution was deposited on the wafer while it lay on a $70\,^{\circ}\mathrm{C}$ hotplate or through freeze-drying (described previously). Finally, a $10\,\mathrm{nm}$ layer of Pt/Pd (80/20) was deposited on the entire wafer, using a *Cressington 208 HR B* sputter coater. No rotation or tilt was used.

Instrument. A *FEI Helios NanoLab DualBeam* with a gallium ion source was used for milling and imaging. The electron and ion beams are positioned with a $52°$ angle between them, and the coincidence point between the two beams gives a working distance of $4.1\,\mathrm{mm}$ for the electron beam. The stage is tilted at an angle of $52°$ during use, which puts the ion beam directly above the sample. The two beams can be operated independently, and each beam is blanked while the other is in use. The instrument is equipped with a conventional ETD detector and TLD detector for use in immersion mode, as well as an an in-column electron (ICE) detector - another ETD detector at a different angle with the added possibility of detecting secondary ions.

To get the sample in position the sample was moved to the eucentric height. The electron beam was centered on a distinct feature before the sample was tilted first to $7°$ and then to $52°$, each time adjusting the height of the stage slightly to realign on the feature. The sample was tiled to place the ion beam directly perpendicular to the sample surface. The ion beam must be aligned with the electron beam, to ensure that the images are corresponding. This was done in an area of little interest, to avoid damage from the ions. The same was done for focusing of the ion beam before milling. As the current changes so does the focus of the beam, such that the beam must be refocus to ensure sharp features.

Milling. Care was taken to avoid damage to the area of interest, as well as curtaining effects. A $200\,\mathrm{nm}$ layer of Pt was deposited on top of the area of interest using the electron beam with an acceleration voltage of $3\,\mathrm{kV}$ and a current of $0.34\,\mathrm{nA}$ [64], before a $0.3\,\mu\mathrm{m}$ layer was deposited using a $93\,\mathrm{pA}$ current [75]. Sometimes a larger segment milled using the ion beam with an current of $2.8\,\mathrm{nA}$ was used to remove material obscuring the area of interest. To expose the area of interest, a narrow regular cross-section was milled at a current of $93\,\mathrm{pA}$ [63]. The porosity of PCC was preserved by omitting a final cleaning cross-section at low current [75]. The milling parameters used were previously explored in detail by Roede [75].

Imaging. The images were captured using mainly SE with the TLD, ETD and ICE detectors. Images were captured both before and after milling. Steps were taken to ensure minimal astigmatism. Multiple acceleration voltages were used, with focus on an acceleration voltages of $3\,\mathrm{kV}$ and $5\,\mathrm{kV}$ combined with a current of $0.34\,\mathrm{nA}$ or $1.4\,\mathrm{nA}$. The selection of imaging parameters was based on work done by Roede [75]. To obtain clear images, some experimentation was done with regard to dwell time.

Chapter 4

Results

All known parameters are documented in this or the preceding section. However, concentration of solutions and/or suspensions after mixing and centrifugation (and often times of samples prepared for optical imaging) are largely unknown. Yield as well as losses incurred during centrifugation and due to the settling of large particles, has not been quantified.

4.1 $CaCO_3$ Template Particles

Spherical $CaCO_3$ particles were achieved by mixing Na_2CO_3 and $CaCl_2 \cdot H_2O$ solutions, and freeze-drying proved successful for maintaining the spherical shape while drying. The spherical shape was confirmed using optical microscopy and SEM, as can be seen in Figure 4.1a and 4.1b respectively. Particle area and thereby diameter was ascertained using optical microscopy. Though multiple images were used, an example of the images and masks used for the analysis can be found in Figure 4.2. The particles were found to range in diameter from $2.50\,\mu\mathrm{m}$ to $8.50\,\mu\mathrm{m}$ with an average diameter of $6.25\,\mu\mathrm{m}$ - this with a SD (standard deviation) of $1.09\,\mu\mathrm{m}$.

The *Malvern Mastersizer Hydro SV* also provided a measure of the particles' average diameter. The particles were investigated before and after treatment in an ultrasound bath for $5\,\mathrm{min}$. Before sonication, multiple measurements provided an average D[4,3] (averaged over multiple measurements) of $16.80\,\mu\mathrm{m}$, with individual measurements showing means as high as $20.60\,\mu\mathrm{m}$ and as low as $10.10\,\mu\mathrm{m}$. After sonication the average D[4,3] (averaged over multiple measurements) dropped to $6.48\,\mu\mathrm{m}$, with the individual measurements reaching a maximum of $7.56\,\mu\mathrm{m}$ and minimum of $5.71\,\mu\mathrm{m}$. It is of note that surface area moment mean diameters

(D[3,2]) can be obtained from the Mastersizer data. However, these values are mathematically derived and thus has a slightly increased uncertainty. The value was seemingly less affected by the ultrasound treatment, with an average D[3,2] (averaged over multiple measurements) before sonication of $6.03\,\mu\mathrm{m}$ and after sonications of $4.99\,\mu\mathrm{m}$.

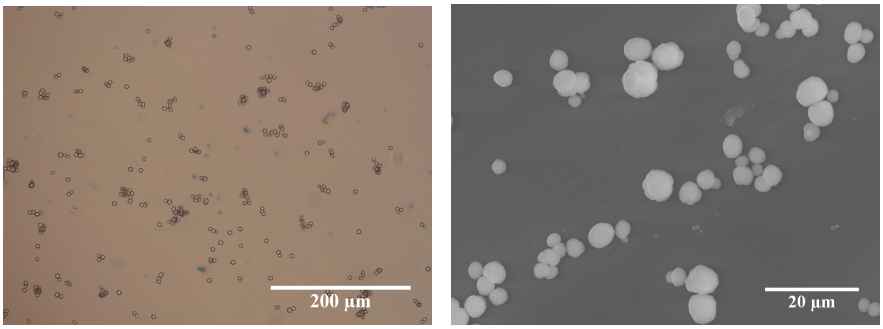

(a) **(b)**

Figure 4.1: Size and shape of PCC particles confirmed using (a) BF optical microscopy and (b) SEM. The SEM micrograph is a SE image captured in immersion mode using an acceleration voltage of $25\,\mathrm{kV}$.

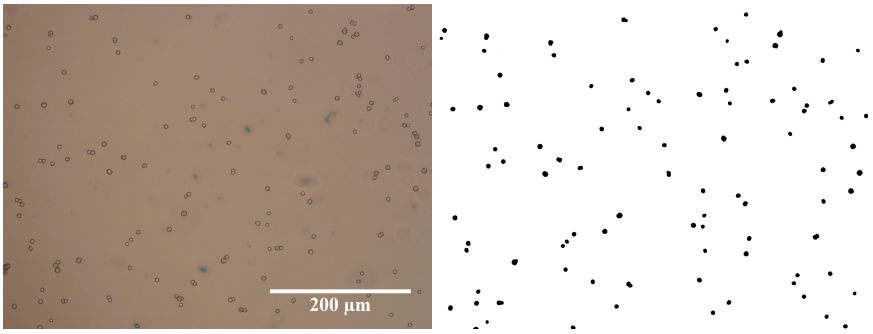

(a) **(b)**

Figure 4.2: Example of using imageJ to find diameter of the PCC particles. (a) shows the BF optical image used for the analysis and (b) the mask extracted from the image.

The morphology of the PCC was investigated using the FIB for milling and SEM for imaging. The spherical shape and pitted surface is clear in Figure 4.3. The internal structure was revealed through milling, as shown in Figure 4.4. In line with the pitted surface, the particles can be seen to exhibit high internal porosity. In both figures, some rhombohedral $CaCO_3$ is present.

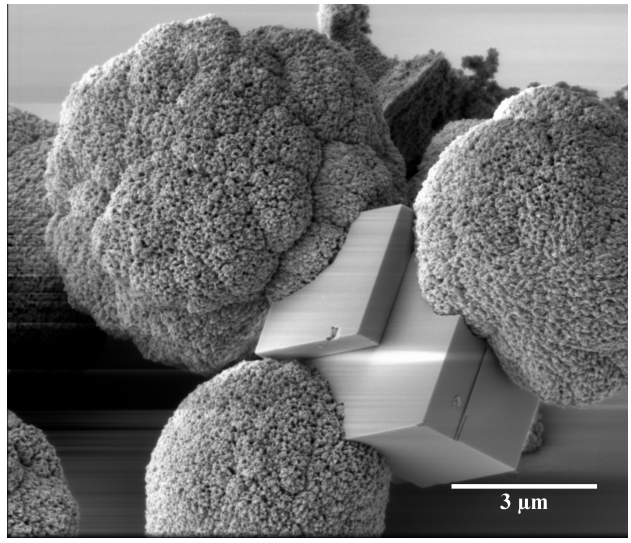

Figure 4.3: SE image showing the pitted surface of PCC particles, made using the mixing method. The image was taken using the ICE detector with an acceleration voltage of $2\,\mathrm{kV}$ and a $0.34\,\mathrm{nA}$ current. This is a composite of 16 images each with a dwell time of $200\,\mathrm{ns}$.

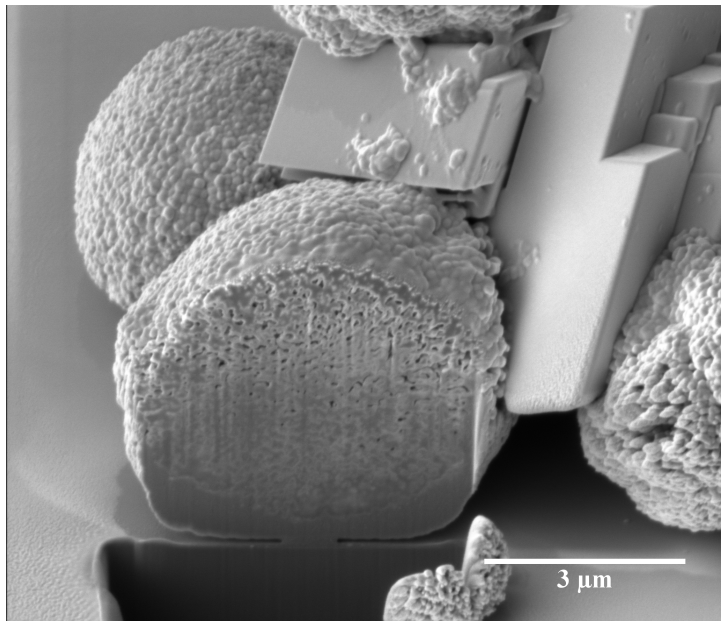

Figure 4.4: SE image showing the porous interior of a PCC particle after ion beam milling. The image was taken using the ICE detector with an acceleration voltage of $2\,\mathrm{kV}$ and a $0.34\,\mathrm{nA}$ current. This is a composite of 16 images each with a dwell time of $1\,\mu\mathrm{s}$.

4.2 Cellulose Nanofibrils

The diameter of the CNF-T fibrils was investigated using AFM images, such as those presented in Figure 4.5. The suspension was dried on mica at either $90\,^{\circ}\mathrm{C}$ or $70\,^{\circ}\mathrm{C}$, to evaluate whether drying temp would affect the diameter measurements. Height data extracted from the image provides average diameters of $2.6\,\mathrm{nm}$ (standard error of $0.11\,\mathrm{nm}$) and $2.8\,\mathrm{nm}$ (standard error of $0.14\,\mathrm{nm}$) respectively. Some diameters were measured to be as small as $1.0\,\mathrm{nm}$. A Wilcoxon rank-sum test confirmed that there was no significant difference between the two temperatures, with a 95% significance. More parameters from the statistical analysis - such as p-values - can be found in Table 2 (Appendix).

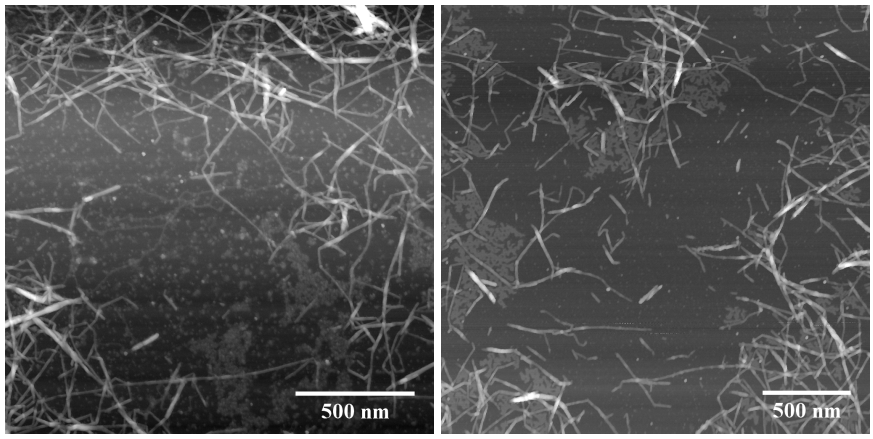

(a) **(b)**

Figure 4.5: Examples of AFM micrographs used to find CNF-T diameter. CNF-T was dried on mica at (a) $70\,^{\circ}\mathrm{C}$ and (b) $90\,^{\circ}\mathrm{C}$. Black pixels denote a height of $0\,\mathrm{nm}$, while white pixels denote $14\,\mathrm{nm}$.

The suspension were found to possess the expected shear thinning properties [31, 48, 76–78]. The effect was strengthened as the concentration of fibrils increased, as is evident in Figure 4.6a. An attempt was made to determine critical overlap concentration in a similar manner as was done by Lasseuguette et al. (2004) [76]. For the double log plot of viscosity as a function of concentration with a shear rate of $1\,\mathrm{s}^{-1}$ (Figure 4.6b), a slight change became apparent at around a CNF-T concentration of 0.17% (w/w). The change in slope is however not as pronounced as was demonstrated by Lasseuguette et al.[76], with a slope change from only 2.1 to 3.3. The slopes are the same as the exponent of equation 2.6, and the terms slope and exponent will be used interchangeably.

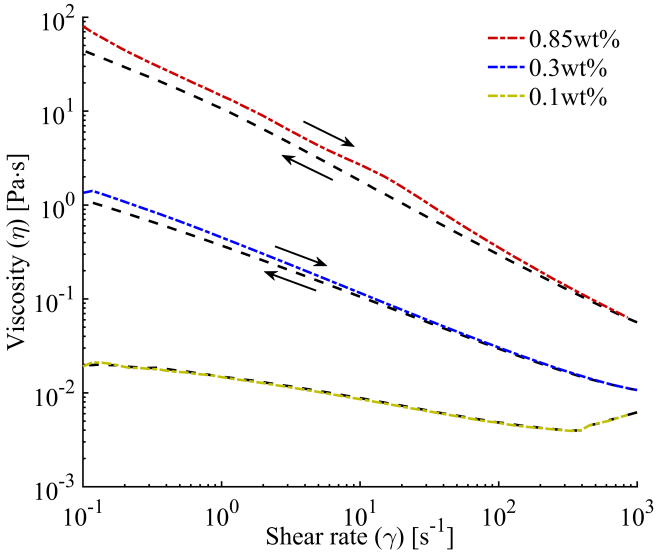

(a)

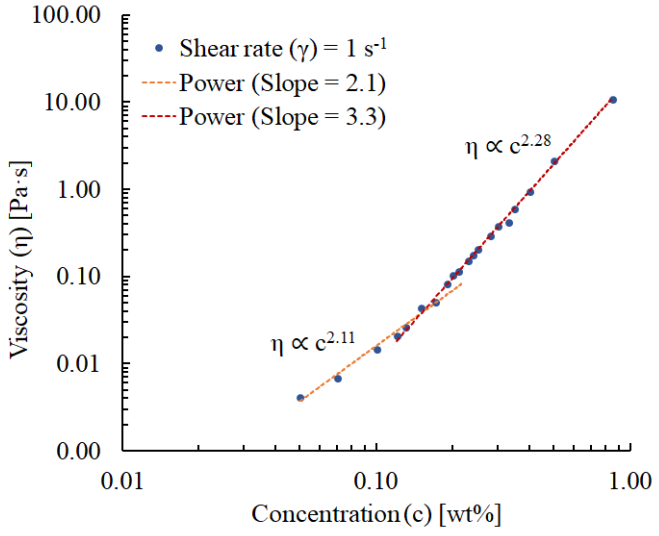

(b)

Figure 4.6: The rheological properties of CNF-T. The double log plot in (a) shows viscosity (η) as a function of shear rate (γ) for CNF-T. The arrows indicate in which direction the shear rate was varied. The double log plot in (b) shows viscosity (η) as a function of concentration (c). The shear rate (γ) for all measurements in (b) was $1\,\mathrm{s}^{-1}$. The curve is fitted with power laws of slope=exponent from equation 2.6. Each point is averaged over 12 measurements. The value of each point with SD can be found in Table 1 (Appendix).

4.3 Microcapsules

The formation of layered capsules was thoroughly investigated. The ζ-potential after interaction between PCC and PDADMAC was found to average $12.4\,\mathrm{mV}$. The less than colloidal conditions caused the potential to trend as a result of sedimentation, such that the absolute value of the potential is likely not correct, but the positive nature of the single layer capsules is apparent. This confirms the formation of a layer of PDADMAC around the PCC particles. The size of the particles in suspension before and after interaction with PDADMAC and subsequent washing, remained largely unchanged. The average D[4,3] (averaged over multiple measurements) was found to be $6.89\,\mu\mathrm{m}$.

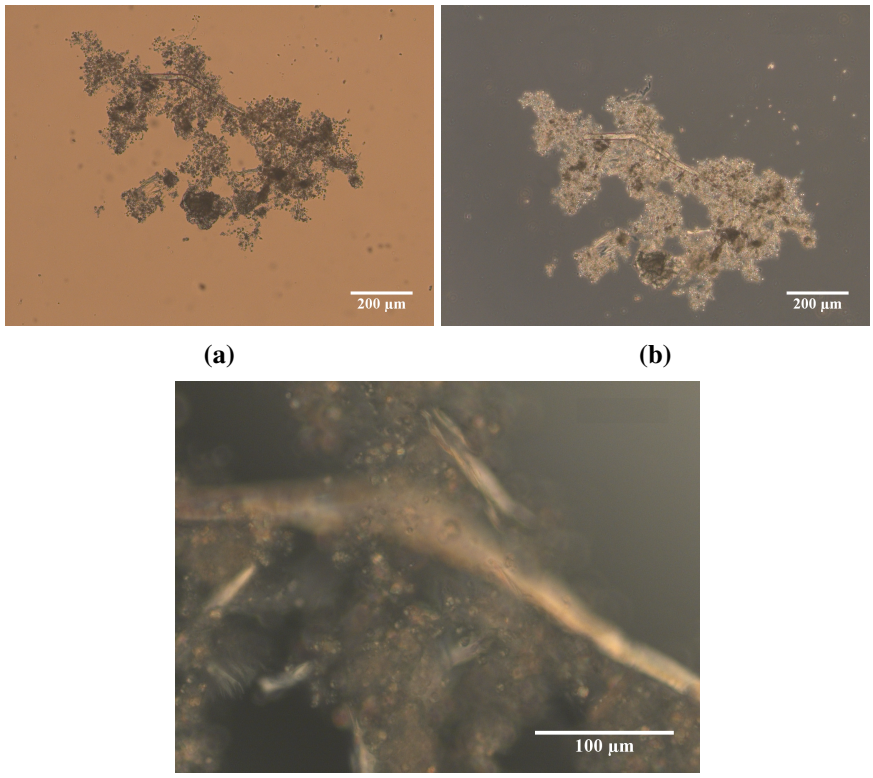

(a) **(b)**

(c)

Figure 4.7: Optical micrographs of microcapsule flocs, where slightly different features are highlighted by (a) BF (b) phase contrast and (c) DIC.

Once the single layer capsules had interacted with CNF-T visual inspection and optical images revealed the formation of larger flocs of PCC and CNF-T (PDADMAC is of course also present). Figure 4.7a appears to show one or two larger fibers with

attached PCC and CNF-T. Further investigation using BF, DIC and phase contrast revealed PCC in large flocs with CNF-T. The CNF-T appears as a foggy white, glassy material in the DIC images (Figure 4.7c), while the edges of fibers became more apparent when BF (Figure 4.7a) and phase contrast (Figure 4.7b) were used. Some larger fibers are clearly shown in Figure 4.7b as the backbone of the flocs. As the concentration of CNF-T was varied, the flocculation behavior changed. When the single layer capsules were added to the the $0.015\,\mathrm{mg}\cdot\mathrm{mL}^{-1}$ CNF-T suspension, the average D[4,3] was $953\,\mathrm{nm}$. As the solution was diluted, the flocculation decreased. CNF-T concentrations of $0.0015\,\mathrm{mg}\cdot\mathrm{mL}^{-1}$ and $0.000\,75\,\mathrm{mg}\cdot\mathrm{mL}^{-1}$ yielded average D[4,3] values of $385\,\mathrm{nm}$ and $120\,\mathrm{nm}$ respectively.

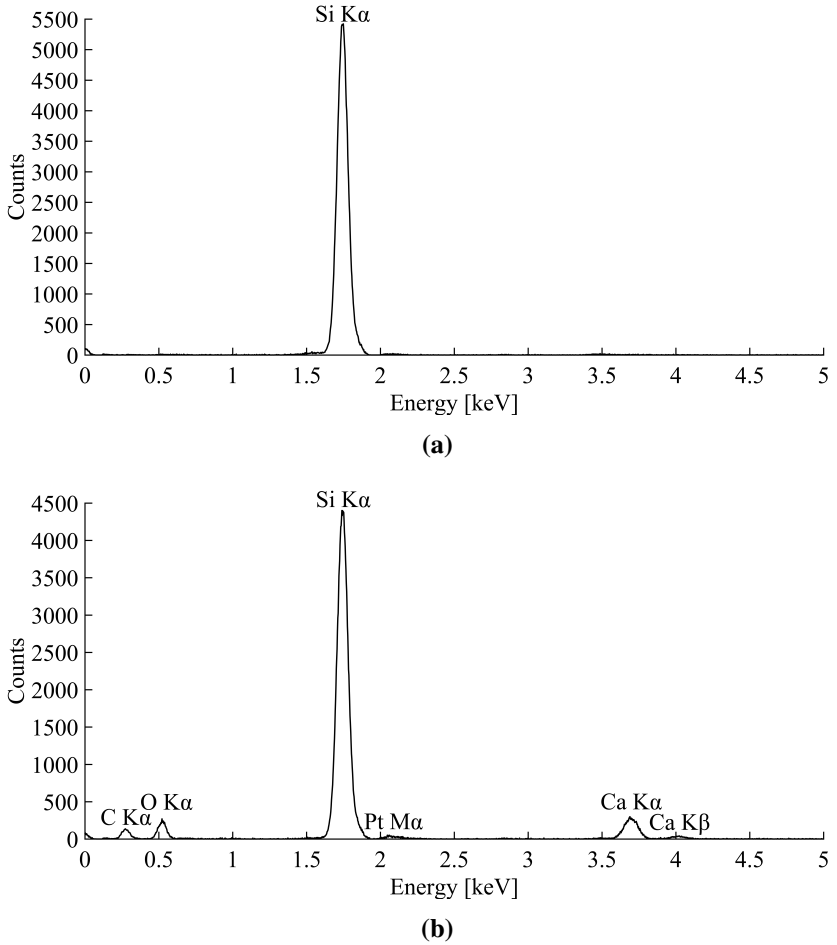

Figure 4.8: EDX spectra comparing (a) an area of clean Si wafer surface to (b) an area of $CaCO_3$.

Further evidence of the interaction behavior between single layer capsules and CNF-T was clear in SEM images. Figure 4.9 shows an overview of a microcapsule floc dried on a plasma cleaned Si wafers at $70\,^{\circ}\mathrm{C}$. Several phenomena are evident in the image. Larger fibers lay on the wafer surface and the PCC (indicated by A) particles are either completely or partially covered by CNF-T (indicated by D and E respectively). Additionally, flat puddle-like structures can be seen in the image (indicated by B). EDX data revealed the presence of Ca in these areas, identifying the "puddles" as $CaCO_3$. An elemental comparison between areas of clean wafer surface and the "puddled" areas is shown in Figure 4.8. When the PCC particles were sectioned using the ion beam the porous interior was revealed (see Figure 4.10).

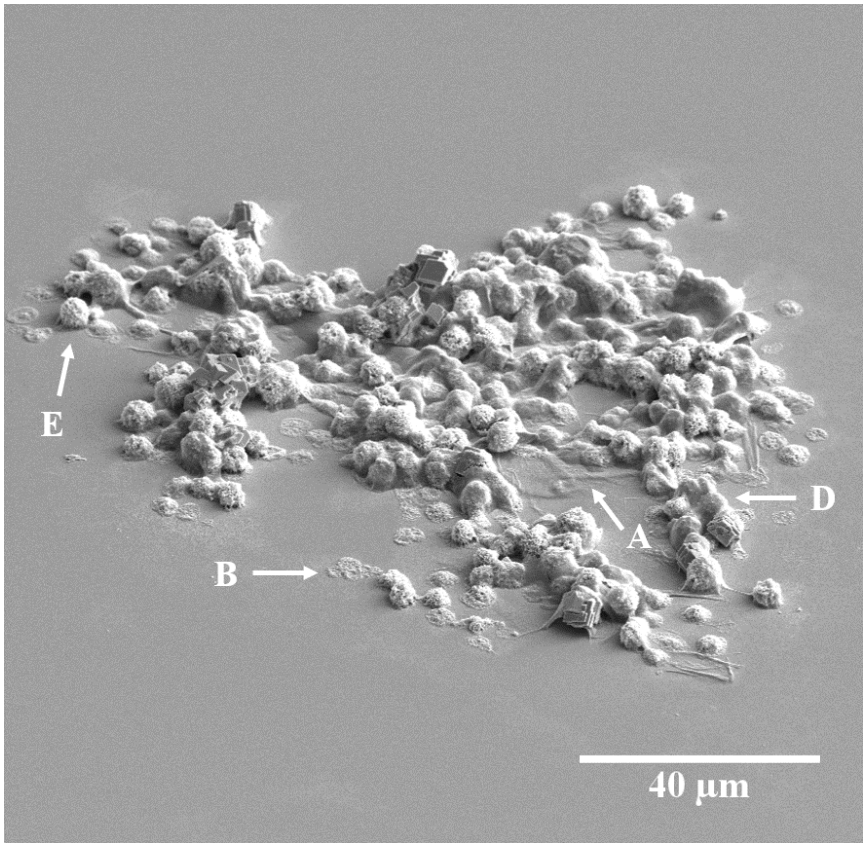

Figure 4.9: SE image showing a microcapsule floc. Areas of interset include CNF-T fibrils on the wafer surface (A), $CaCO_3$ "puddles" (B) and PCC particles either completely (D) or partially (E) covered by CNF-T. The image was taken using the ETD detector with an acceleration voltage of $5\,\mathrm{kV}$ and a $0.34\,\mathrm{nA}$ current, captured using a $10\,\mu\mathrm{s}$ dwell time.

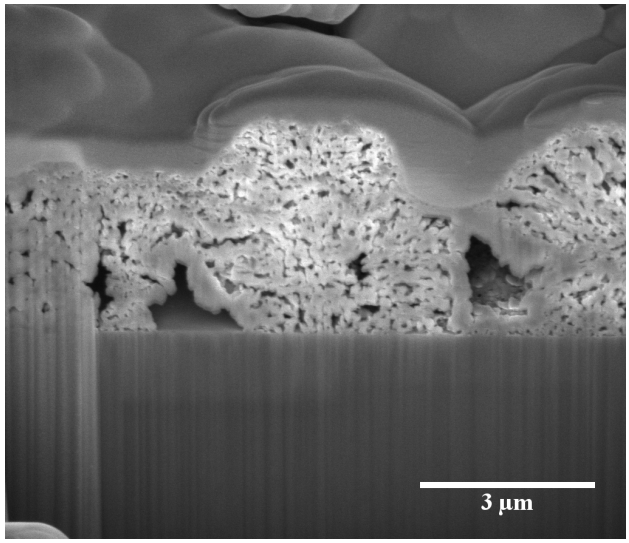

Figure 4.10: SE image of a section of a microcapsule floc exposed by FIB milling. The image was taken using the TLD detector with an acceleration voltage of $5\,\mathrm{kV}$ and a $0.34\,\mathrm{nA}$ current, captured using a $10\,\mu\mathrm{s}$ dwell time.

STEM images reveal much the same as the SEM images, with the added benefit of more clearly distinguishing between CNF-T and PCC. Figure 4.11 shows a comparison between DF-STEM images taken at a detector angle of $10°$ (Figure 4.11a), $40°$ (Figure 4.11b) and $55°$ (Figure 4.11c). The image at $10°$ detector angle clearly shows the fibrous network laying on the holey carbon film and wrapping around one of the particles. As the angle increases the visibility of CNF-T decreases and the contours of the PCC particles become more apparent. Areas of interest in each image are indicated by arrows.

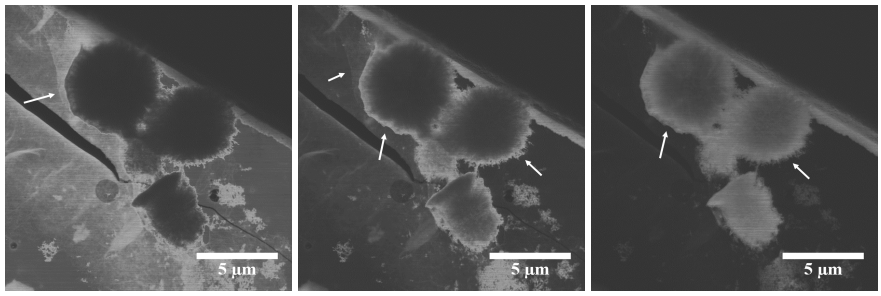

(a) **(b)** **(c)**

Figure 4.11: DF-STEM micrographs captured with an acceleration voltage of $20\,\mathrm{kV}$. The detector angle was varied between (a) $10°$, (b) $40°$ and (c) $55°$, to illustrate the effect this would have on Z contrast.

SE images of the corresponding area to Figure 4.11 were captured. The two images in Figure 4.12 are taken with an acceleration voltage of 15 kV and 30 kV respectively. Figure 4.12a shows more of the CNF-T layer that has formed around the PCC particle, while Figure 4.12b shows the outlines of the PCC particle more clearly.

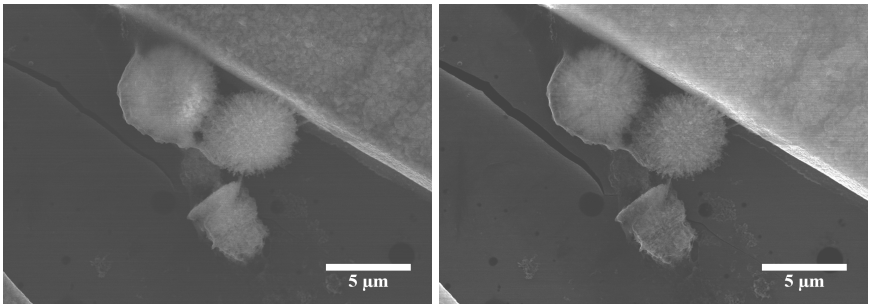

(a) **(b)**

Figure 4.12: SE images of the same area as seen in Figure 4.11, illustrating that changing the acceleration voltage changes imaging depth. The images are captured with an immersion microscope at (a) 15 kV and (b) 30 kV acceleration.

4.3.1 Troubleshooting

The supernatants from the the third and an added fourth wash cycle were examined for their role in the flocculation behavior of the CNF-T suspensions. The fourth wash cycle was added to ascertain whether extra washing steps would lead to any change in behavior. When the respective supernatant were combined with a solution saturated with $CO_3{}^{2-}$ beyond the supersaturation of $CaCO_3$, there was no evidence of $CaCO_3$ precipitation. However, when the respective supernatants were added drop-wise to CNF-T suspensions in similar amounts as when adding washed single layer capsules, flocculation became evident within a few minutes of the addition. There was no discernible difference between the wash cycles.

4.4 Freeze-Drying Using Liquid N_2

Freeze-drying of the microcapsules with cooling using liquid N_2 was performed to test the efficacy of this as a drying technique for microcapsules made with CNF-T. The drying process yielded structures similar to those found in an aqueous environment using optical microscopy and dried using SEM. The main difference of the freeze-dried with respect to the hotplate dried samples was the more native appearance of the capsules. Some results can be seen in Figure 4.13. Larger fiber surfaces with multiple PCC particles attached, can be seen. The samples were milled using the ion beam. The porous structure of PCC was again revealed, but

no evidence of CNF-T pulling away from the surface of PCC while drying was found. Figure 4.15 does shows cellulose curving under the PCC particles, and though the dried CNF-T appears to span the pores of the particle, it has not pulled away. In other areas the CNF-T forms a more network-like structure than a capsule around PCC. Additionally, highly porous network structures seemingly containing some individual fibrils were discovered (Figure 4.14).

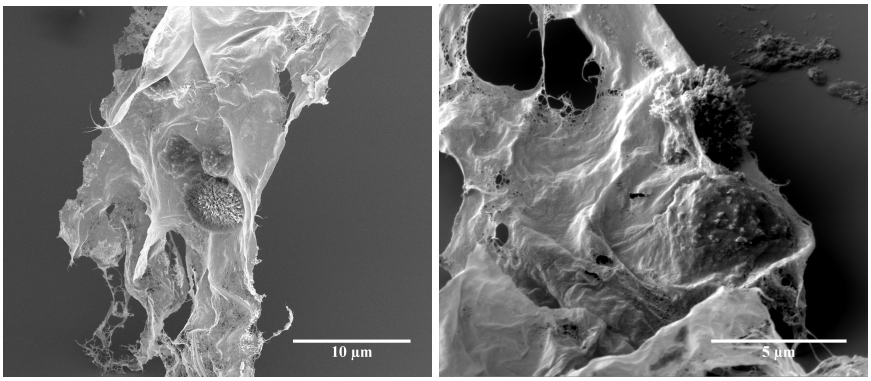

(a) **(b)**

Figure 4.13: SE images of microcapsule flocs cooled with liquid N_2 before freeze-drying. Images are captured with (a) $5\,\mathrm{kV}$ and (b) $3\,\mathrm{kV}$ acceleration using the TLD and ICE detectors respectively. The current was set to $1.4\,\mathrm{nA}$, with a dwell time of $10\,\mu\mathrm{s}$.

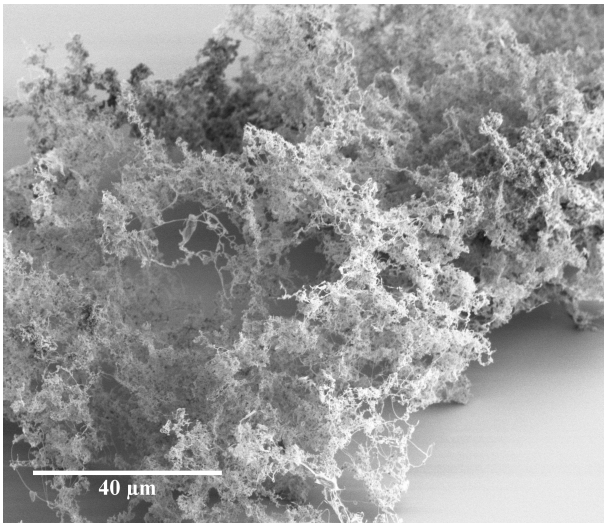

Figure 4.14: SE image of CNF-T cooled with liquid N_2 before freeze-drying. The image was taken using the ETD detector with an acceleration voltage of $3\,\mathrm{kV}$ and a $0.34\,\mathrm{nA}$ current. The resulting image is a composite of 16 images captured with a $200\,\mathrm{ns}$ dwell time.

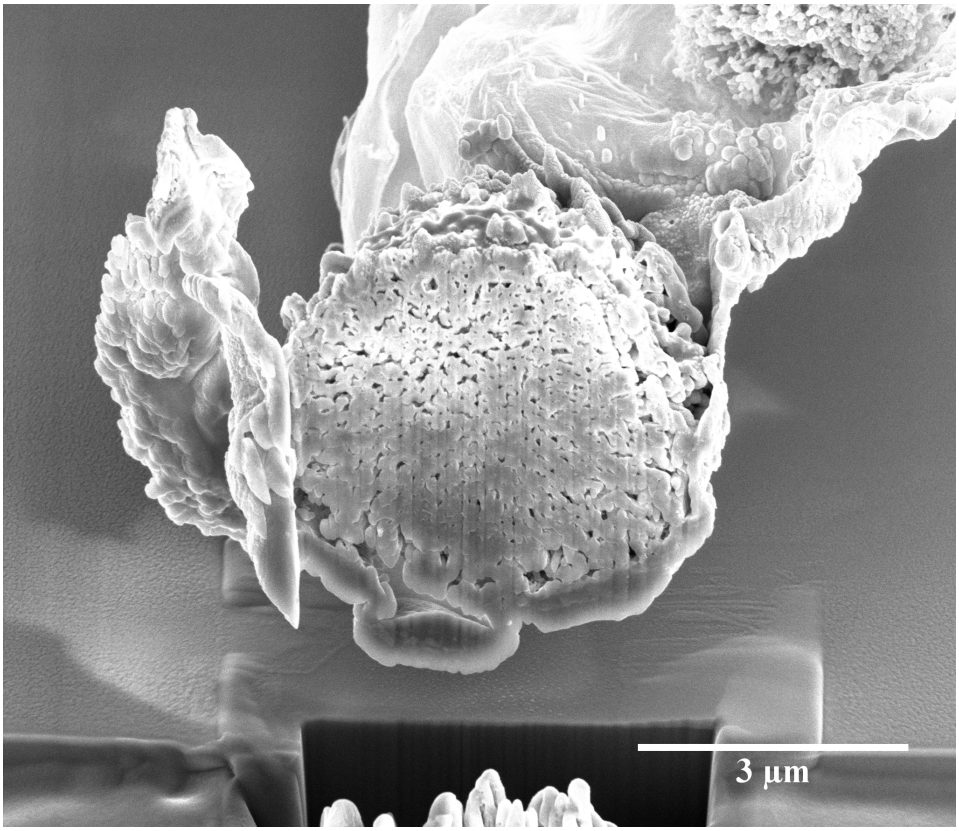

Figure 4.15: SE image of a section of a microcapsule floc cooled with liquid N_2 before freeze-drying. The area was exposed through FIB milling. The image was taken using the TLD detector in immersion mode with an acceleration voltage of $5\,\mathrm{kV}$ and a $1.4\,\mathrm{nA}$ current. A $10\,\mu\mathrm{s}$ dwell time was used.

Chapter 5

Discussion

The results presented previously will in this chapter be discussed in detail and further elaborated upon. Some sugestions for further work will be presented and discussed.

5.1 $CaCO_3$ Template Particles

Two methods were used to examine PCC particle diameter. The first was optical microscopy images, the diameters obtained are a result of looking at the projected area of the particles. When this method of analysis is reviewed, some uncertainty may be connected to agglomerates of two or three of the smaller particles. The resulting average diameter may be slightly skewed towards larger diameters.

The second method for determining particle diameter was scattering. This method gave the volume moment mean diameter (D[4,3]). While larger agglomerates could be excluded from the optical measurements by specifying roundness parameters and excluding excessive sizes during analysis, this was not possible for the scattering measurements. Initially these measurements provided a D[4,3] mean of $16.80\,\mu\mathrm{m}$, with a large variation in the individual measurements. After 5 minutes of treatment in an ultrasound bath, the mean fell to $6.48\,\mu\mathrm{m}$. The D[4,3] is particularly sensitive to few large particles, due to its volume dependency, implying that there were more large particles present in solution before versus after sonication [49]. It is inferred that the sonication served to break up agglomerates PCC particles. Unfortunately the way the Mastersizer software expresses data, it was not possible to do statistical analysis of the values in question, and any comparisons are purely speculative. The inference still informs the decision to sonicate the PCC particle suspensions before mixing with PDADMAC solutions, in an effort

to minimize agglomeration due to the unstable nature of the PCC suspension.

It is important to be aware that the diameters measured using the two separate techniques (Mastersizer and image analysis) can not be directly compared. The D[4,3] has a volume dependence, whereas the diameter derived from images has an area dependence [49]. As noted, the D[3,2] can be derived from the scattering data, with a slightly elevated uncertainty [49]. The D[3,2] value has an area dependence, but this area is the particle surface area as apposed to the projected area used for determining diameters using image analysis software. Image analysis yields a mean diameter known as D[2,0], which is dependent on the number of particles (which moment means are not). Though the average diameters found by scattering and image analysis cannot be compared directly, the two techniques yielded analogous average diameters of $6.48\,\mu\mathrm{m}$ and $6.25\,\mu\mathrm{m}$ respectively.

Though ζ-potential of the PCC particles was attempted investigated, this proved difficult due to the less than colloidal conditions and tendency to agglomerate. The potential could provide an future indication of layer formation, through charge reversal [25, 26, 70, 73, 74]. However, Volodkin et al. (2004) made particles using identical parameters resulting in particles with average diameters ranging from $4\,\mu\mathrm{m}$ to $6\,\mu\mathrm{m}$ [74]. These particles were found to have a ζ-potential of $-12.2\,\mathrm{mV}$, leading to the conclusion that particles made in this manner bear a negative charge [43, 74]. Henceforth this will be assumed to be true. Had this not been the case, the choice of PDADMAC as the second polymer layer would have proven redundant.

The need for freeze-drying to maintain particle shape during drying, is testament to the instability of the particles. The spherically shaped particles are likely to be vaterite [17, 65, 79], which is a metastable phase [80]. If heat is added to a suspension diffusion increases [47], allowing the particles to grow by aggregation and Ostwald ripening at a very fast rate [34]. Any change in morphology is most likely the result of a phase change, where vaterite is transformed into the more stable calcite - know to have a more cubic morphology [80]. The instability of the spherical phase leads to freeze-drying being required to maintain spherical morphology while drying. The instability of the particles was confirmed by SEM imaging after 4 months of storage in a dry container. The presence of small ammounts of moisture was enough for the morphology of some of the particles to change to rhomobohedral. This change has been captured in Figure 5.1, and is also visible in Figures 4.3 and 4.4.

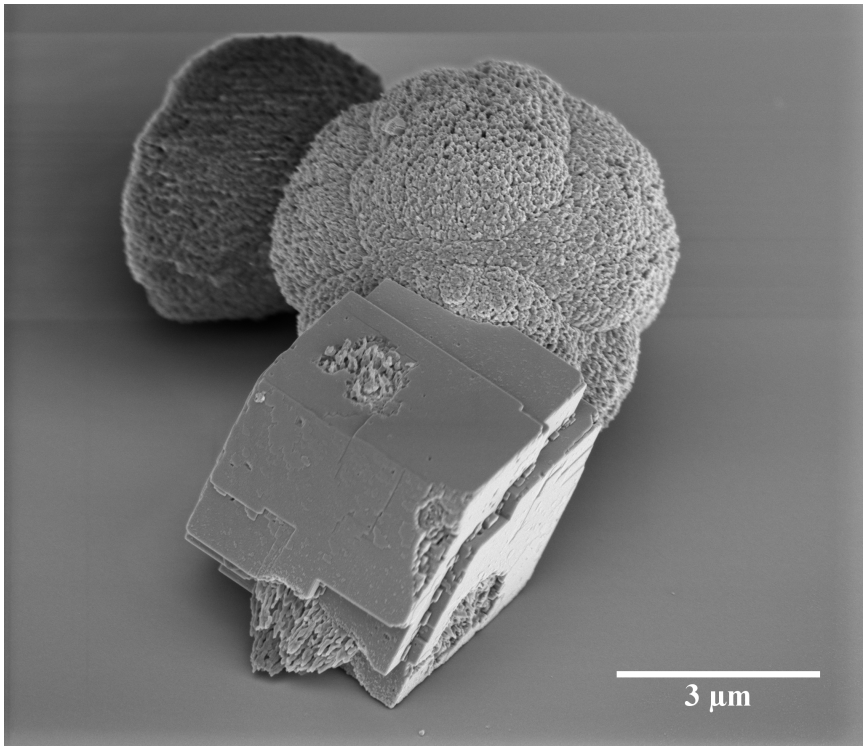

Figure 5.1: SE image showing PCC in the process of transitioning from vaterite to calcite. The image was taken using the TLD detector in immersion mode. The acceleration voltage used was $2\,\mathrm{kV}$ combined with a $0.17\,\mathrm{nA}$ current. The resulting image is a composite of 16 images captured with a $1\,\mu\mathrm{s}$ dwell time.

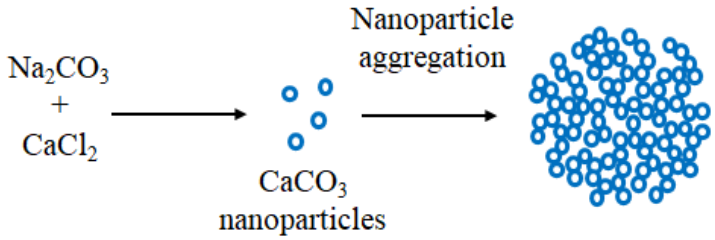

Figure 5.2: Illustration of one suggested $CaCO_3$ precipitation scheme. Adapted from [81].

Once the internal structure was revealed, it became clear that the PCC particles were highly porous (Figure 4.4). Volodkin et al. (2004) suggests that this is the result of an initial formation of nanoparticles which aggregate to form larger porous microparticles [81]. This a common scheme presented in literature. The suggested

scheme is visualized in Figure 5.2. Andreassen (2005) has on the other hand argued that the particle structure is more congruent with spherulitic growth [82]. This theory better explains the radial symmetry of dissolution seen in Figure 5.5e, where the surface resembles a collection of needles extending from a central point after some time in solution [79].

The imaging of the particles plays an important a role in how the internal structure is visualized. When an ion beam is used for milling, material removed by the beam will be redeposited on the sample [64]. Some material may be redeposited in the pores, creating the illusion of less porosity than was initially present. It is pertinent to keep this in mind when viewing images of porous materials exposed through ion milling.

5.2 Cellulose Nanofibrils

The average diameter found for the CNF-T fibrils was lower than expected. The same stock suspension was previously investigated by Ottesen et al. (2017) The diameter was then concluded to be about $5\,\mathrm{nm}$, when analyzing data from both AFM and TEM measurements [67]. The exact same samples were reexamined using AFM, and the average diameter was found to be $3.9\,\mathrm{nm}$ with a standard error of $0.14\,\mathrm{nm}$. None of the measured fibrils approached a diameter of $1\,\mathrm{nm}$. The samples used by Ottesen et al. were dried at $70\,^{\circ}\mathrm{C}$. Selected images of the new samples dried at $70\,^{\circ}\mathrm{C}$ and $90\,^{\circ}\mathrm{C}$ are presented alongside an updated image of the samples used by Ottesen et al. in Figure 5.4. A qualitative assessment can be made by looking at the box plot in Figure 5.3. A Wilcoxon rank-sum test confirmed that there was a significant difference between the two samples dried at $70\,^{\circ}\mathrm{C}$, with 95% confidence. The change could be a consequence of local variations within the stock suspension, resulting in the measured sample containing more smaller

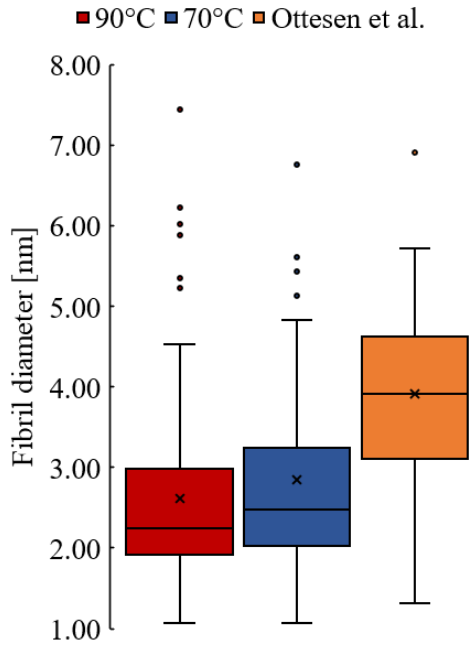

Figure 5.3: Box plot comparing CNF-T fibril diameters measured using AFM.

fibrils. Another explanation could lie in degradation over time, as the suspension was stored for over a year. Though the measured diameter is deemed to be unexpected, similarly small diameters have previously been found under analogous circumstances [28, 72].

It is an interesting result that there was no significant difference in the fibril diameter between drying the samples at $70\,^{\circ}\mathrm{C}$ and $90\,^{\circ}\mathrm{C}$. The difference may or may not become significant if lower drying temperatures were compared. The diameter is extracted from hight profiles to mitigate artifacts caused by tip convolution. So it can be speculated that one could see an increase in fibril diameter as the drying temperature was reduced, which is deduced from the fact that lower drying temperature would mean slower drying. This in turn would create less pull from capillary forces as the water evaporated, so could result in less compression of the fibrils [47]. This may also not be the case, as similar fibril diameters were found by Rodionova et al. (2013) upon drying at $22\,^{\circ}\mathrm{C}$ [72]. Drying temperature may have little overall effect on diameter measurements.

When considering the rheological properties of CNF-T, several studies have demonstrated similar slopes to those in Figure 4.6b. To this effect Naderi et al. (2014) reported exponents of 2-2.4 and Shogren et al. (2011) reported exponents of 3.2-3.7 at a shear rate of $1\,\mathrm{s}^{-1}$ [77, 78], among others [48]. Note that the CNF qualities and batches are not consistent between these sources. Further, none of these have pointed to a specific change in exponent. A direct comparison becomes difficult.

The lack of a clear change in slope seen in the double log plot of viscosity as a function of shear rate in Figure 4.6b, is likely partially related to the use of a higher shear rate than that used by Lasseuguette et al. (2004) [76]. Lasseuguette et al. concentrated on the low shear rate of $0.1\,\mathrm{s}^{-1}$, and could then demonstrate a pronounced slope change from 1 to 6 around the cellulose concentration of 0.2% (w/w). The choice to not use a similarly low shear rate was based on the high uncertainty and large hysteresis seen at these values (Figure 4.6a). The uncertainty is an inherent limitation of the instrument. The uncertainty is most pronounced for lower CNF-T concentrations, while the hysteresis becomes very large for higher concentrations. Lasseuguette et al. do however include plots of viscosity as a function of concentration also for other shear rates, among them $1\,\mathrm{s}^{-1}$ [76]. At this shear rate a more subtle change in exponent appears closer to 0.3% (w/w) of cellulose. From this, it can be speculated that the demonstrated slope change at 0.17% (w/w) of CNF-T at $1\,\mathrm{s}^{-1}$ might become more pronounced and appear at a somewhat lower CNF-T concentration for lower shear rates. The less pronounced change in slope at lower CNF-T concentration is more in line with that seen by Tanaka et al. (2014), who also used somewhat higher shear rates [83]. Finally, as properties can vary greatly between batches of CNF, decreasing the concentration

further could reveal a more distinct and lower critical concentration.

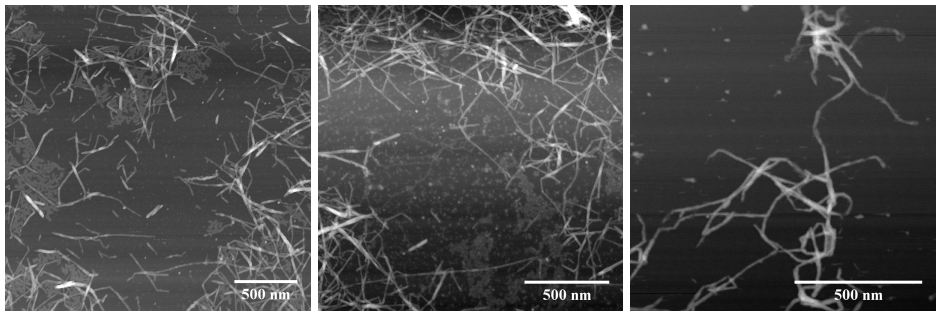

(a) **(b)** **(c)**

Figure 5.4: Examples of AFM micrographs used to compare CNF-T diameters. CNF-T was dried on mica at (a) 90 °C and (b,c) 70 °C. (a,b) Black pixels denote 0 nm, while white pixels denote 14 nm. (c) Black pixels denote 0 nm, while white pixels denote 10.5 nm. In the case of (c) the sample were used by Ottesen et al. (2017) and had been stored for some time before imaging [67].

The purpose of performing rheological studies, was to determine a concentration above which a 3D gel network would begin to form [31]. The change would happen at what is know as the critical overlap concentration, demonstrated by a change in the slope of the double log plot of viscosity as a function of concentration [76]. At the critical overlap concentration it was posited that there would be excessive agglomeration of any microcapsules with CNF-T as the outer layer. Given this reasoning, only the approximate amount of CNF-T needed to cover the surface of the PCC particles was used, thus circumventing washing involving centrifugation. Centrifugation would result in a high concentration being reached in the precipitate. It would also be imperative to stay below such a gelation concentration when initially adding single layer capsules to CNF-T suspension. If 0.17% (w/w) is assumed to be the critical concentration, this was achieved by a large margin.

5.3 Microcapsules

ζ-potential was not only measured for PCC particles in suspension, but measurements became possible after interaction with PDADMAC. The suspension was no more colloidal than before the addition of PDADMAC, but after addition of the positive polymer the suspension appeared to stabilize some [81], thus allowing for measurements. The fact that the absolute value trended, speaks to there still being instabilities present in the system. More precisely large particles sediments and in this way distorting the measurements. As previously stated, charge reversal when studying PEMs indicates layer formation [25, 26, 70, 73, 74]. The positive nature of the ζ-potential after interaction between PCC and PDADMAC points to a coating layer of PDADMAC forming around PCC. Calling the product a single layer capsule is thus appropriate.

The observed decrease in flocculation behavior associated with decreasing CNF-T concentration was as expected, since a decrease in concentration is generally associated with a decrease in bridging flocculation [45, 47]. Limitations to volume and concentration halted further exploration along this avenue. In the $0.000\,75\,\mathrm{mg}\cdot\mathrm{mL}^{-1}$ CNF-T experiment, $5\,\mathrm{mg}$ of PCC was added to $1\,\mathrm{L}$ of CNF-T suspension. To further explore the effects of concentration on flocculation, the added amount of PCC would have to be decreased or the volume of the CNF-T would have to be increased. Both these methods would in effect reduce the concentration of PCC and thereby microcapsules. Eventually the concentration would become too low for diameter measurement using the Mastersizer, limiting the practicality of this approach.

The flocculation in the system may also be the result of something present in the supernatant after washing the single layer capsules. If a certain amount of Ca^{2+} ions were present, this could disrupt the charge balance and cause flocculation [47]. Since no $CaCO_3$ precipitate was found when adding $NaCO_3$ to the supernatant, there is no large amount of leached Ca^{2+} and leaching is likely not the cause. Yet when the supernatant was combined with the CNF-T suspension, flocculation occurred. PDADMAC will adsorb onto the onto the surface of cellulose fibers/fibrils [84]. Interaction between cellulose and polyelectrolytes is known to lead to flocculation, either by decreasing the repulsive forces or by bridging [85–87]. Most probably both mechanisms are at play [87]. An additional fourth wash cycle was added in an attempt to remove more excess PDADMAC than was possible with three wash cycles, but was deemed to not be effective in changing the flocculation behavior. Clearly some excess PDADMAC will always be present in the system.

Figure 5.5c showing dried microcapsules, reveals multiple interesting phenomena. Figure 5.5a is a magnified image showing characteristic nanocellulose fibril structure. The fibrils form continuous sheets with a rough surface. The interaction between PCC and CNF-T tending towards capsule formation is clear in Figures 5.5d and 5.5e. Two different phenomena are evident. Some PCC particles appear to be entirely covered by a layer of CNF-T (Figure 5.5d), while others are covered with a very porous network of CNF-T (Figure 5.5e). The network of CNF-T became very clear in the enlarged images. Only a single layer of CNF-T has been used (a total of two layers of polyelectrolyte), while Volodkin et al. saw very porous networks even after 6 rounds of polyelectrolyte adsorption [74]. With this in mind, the depicted porous structure becomes expected. The CNF-T fibrils appear to span the pores of PCC. The ability of nanocellulose to span large crevices has been previously shown [67]. However, no fibers pulling away from the surface were observed. The puddle-like structure displayed in Figure 5.5b could be either partially dissolved PCC particles or dissolved $CaCO_3$ redeposited as the water evaporates off of the sample. Most likely a combination of the two has occurred.

Complimentary observations were made using STEM (Figure 4.11). Given that changing the detector angle changes the material contrast of the DF images, it follows that this could be use to better observe the interface between PCC and CNF-T. The images in Figure 4.11 are complimentary to those taking taking using SEM, in so far as showing a network structure of CNF-T wrapping around PCC particles. The SE images captured in the same area with two different acceleration voltages (Figure 4.12), provides yet another avenue of investigation. As the acceleration voltage is increased the surface sensitivity of the electron images is decreased [58]. At higher acceleration voltages more of the structures found below the outer CNF-T layer become visible, providing additional valuable insights.

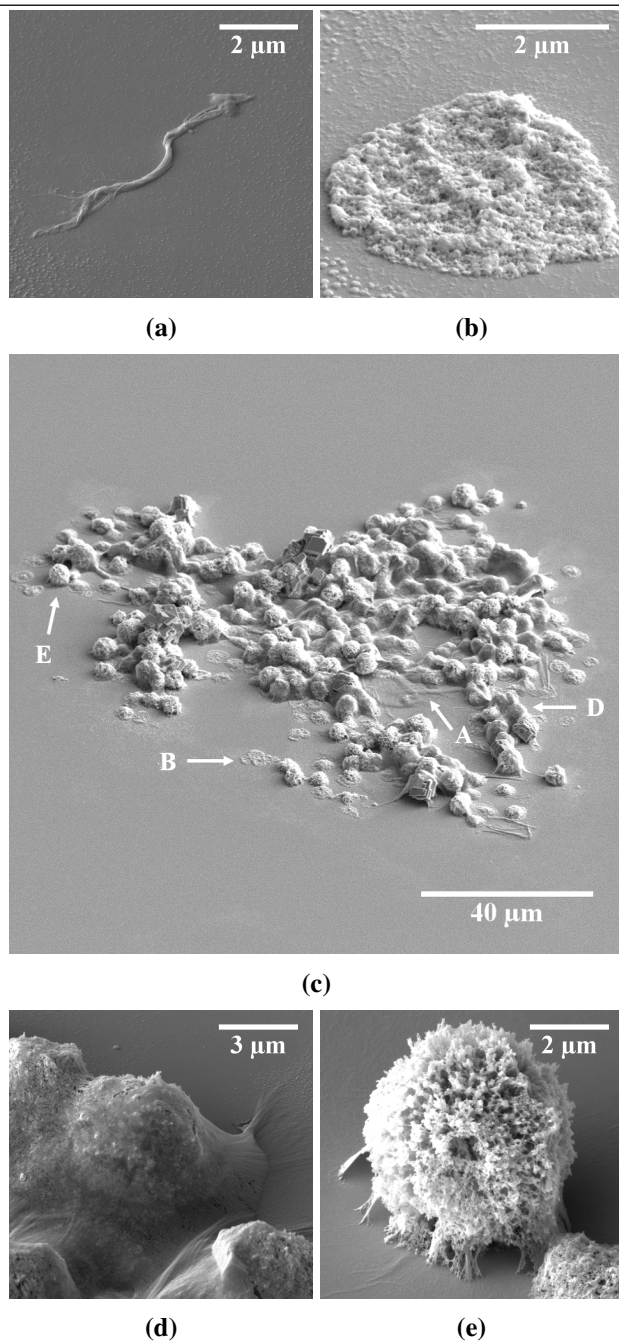

Figure 5.5: SE image showing a microcapsule floc. Areas of interest include (a) CNF-T fibrils on the wafer surface (indicated by A), (b) $CaCO_3$ "puddles" (indicated by B) and PCC particles either (d) completely (indicated by D) or (e) partially (indicated by E) covered by CNF-T. The images were taken using the ETD or ICE detector with the parameters $5\,\mathrm{kV}$ acceleration, $0.34\,\mathrm{nA}$ current, and $10\,\mu\mathrm{s}$ dwell time.

5.4 Freeze-Drying Using Liquid N_2

Rapid vitrification using liquid ethane was shown by Torstensen et al. (2018) to preserve morphology more representative of that of the CNF-T suspensions than could cooling in liquid N_2 [28]. For this study it was however more interesting to look at continuous layers of CNF-T, and liquid N_2 seemed to correspond better with this aim [88]. As previously stated, Figure 4.13 clearly show continuous films in combination with PCC. Freestanding films of CNF-T were also abundant. The films were accompanied by structures more reminiscent of the individual fibrils seen by Torstensen et al. when cooling in liquid ethane [28] (Figure 4.14). It can be speculated that the large difference in concentration between the samples makes it more likely for individuate fibers to not be pushed together by ice crystals forming while cooling [28, 88].

Freeze-drying samples prior to imaging provides images that are better representations of the capsules in suspension. Some samples were freeze-dried before being milled with FIB to expose a surface for imaging. Figure 4.15 points to the importance of the drying step for imaging. In contrast to drying the samples directly onto an Si wafer (Figure 4.10), the freeze-dried samples clearly showed CNF-T curving beneath the PCC particles. When drying directly on a wafer, CNF-T may become compressed. There is also the added danger that the CNF-T dried on top of PCC was not bound to the particles in solution, but was simply deposited on the surface as the sample dried. Freeze-drying, especially with liquid N_2 cooling provides proof that the bond was formed prior to drying.

5.5 Imaging

When using imaging techniques the observer must first establish which materials are present. The porosity revealed in Figure 4.4 combined with the EDX data (Figure 4.8) serve as a guide for locating PCC in the images captured using SEM. The porosity serves as another guiding attribute comparing e.g. Figures 4.4 and 4.10. The particles also show a distinct spherical shape, previously likened to needles extending from a central point, which can further serve as a reference. Figure 5.6a is a DF optical image showing PCC particles with no additives, while Figure 5.6b shows PCC after interaction with PDADMAC and CNF-T. The PCC displays very distinct edges, and thus it is possible to locate PCC also in the optical images. Additionally, any fibrous or network structure is assumed to be CNF-T. SEM images - such as Figure 5.7 - of flocs, where all steps that include PDADMAC have been excluded from the process, bear out this assumption. PDADMAC does not seem to appear clearly in the images. As such, distinguishing between PDADMAC and CNF-T does not have to be considered.

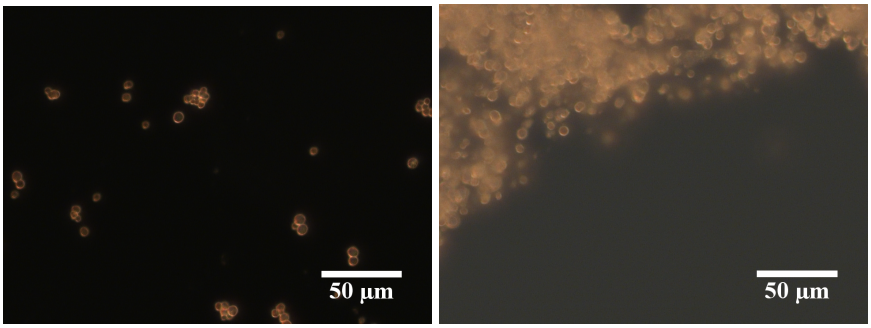

(a) **(b)**

Figure 5.6: DF images illustrating how PCC was located in the optical micrographs, where (a) shows a sample containing only PCC and (b) is taken after interaction with PDADMAC and CNF-T.

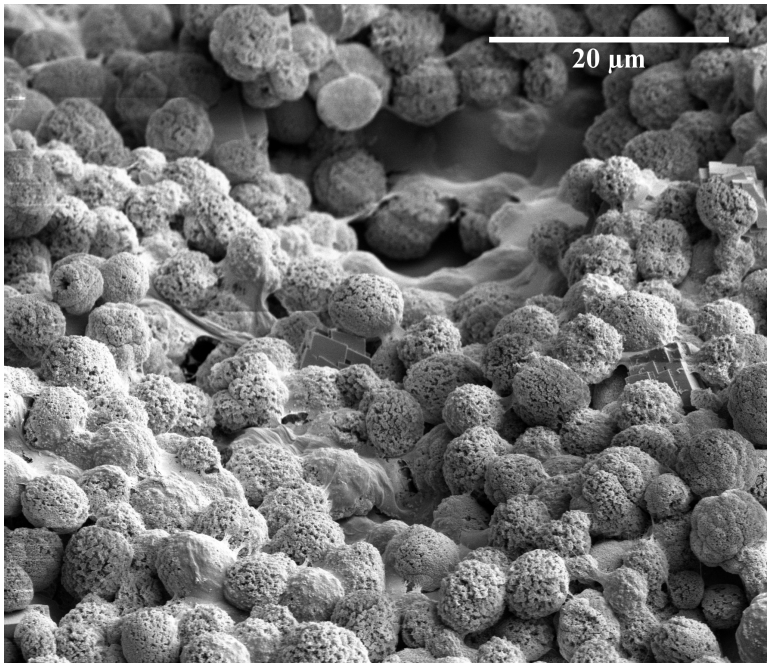

Figure 5.7: SE depicts the resulting large flocs after mixing only PCC and CNF-T. The image was taken using the ETD, with an acceleration voltage of $3\,\mathrm{kV}$ combined with a $0.34\,\mathrm{nA}$ current. The resulting image is a composite of 16 images captured with a $200\,\mathrm{ns}$ dwell time.

The method of imaging has been varied throughout. Each technique has individual benefits and challenges. Using FIB/SEM for imaging paper and cellulose was thoroughly investigated by Roede [75]. The major benefit of using this technique

is the possibility of looking at the interior of the microcapsules. This has as stated been used to locate PCC on the samples, and can - as a full CNF-T capsules forms - be used to look at the behavior of the CNF-T capsules with respect to the template particles. This is the longterm aim of the study. However, there are several drawbacks to the technique, chief of which is the need for high energy ions for milling. Sample prep is complicated by the need for adding an initial Pt/Pd layer though sputtering as well as depositing further Pt layers in situ. The electron beam is used to deposit a primary in situ layer to avoid damage from the beam when depositing a thicker Pt layer with the ion beam [75]. This speaks to the very destructive nature of the ion beam. Although milling using an ion beam reveals the interior of the structures, care has to be taken when interpreting images. Redeposition of milled material and curtaining effects distort the images, but steps taken when imaging - such as adding at Pt top layer and milling in a directional fashion - helped mitigate these problems [64].

Using simply an electron beam avoids some of the problems associated with the high energy ion beam. However, this limits the exploration to the surface of the sample. Figure 4.11, 4.12 and 5.5 shows the merits of such exploration. By varying the sample current Figure 4.12 shows how some internal structure can be revealed. This is however limited by the acceleration voltage. The electron beam will also affect the sample to some degree, and would eventually cause damage. Polymers, having low molecular weight, flexible structures, minimal charge carrying capacity and low melting point, are most susceptible to electron beam effects. The biggest problems would be associated with the melting point, where the electron beam could cause irreversible damage [46]. The damage increases as the imaged area decreases, so if higher acceleration voltages are desired the area imaged should be larger. Interestingly, Figure 4.12b didn't result in damage to the sample which could be due to the large area imaged [60]. An additional problem associated with using an electron beam for imaging is charging, as explained in equation 2.26. To allow for some charge to be carried away, the samples for use in the FIB/SEM were coated with a layer of Pt/Pd. This is not possible when using STEM, since the technique relies on the possibility for transmission of the electron beam. The more material obstructs the beam, the fewer details can be seen. Furthermore, the atomic number contrast generated by varying the detector angle would no longer be correct. In essence, STEM can be used to look at the interface between CNF-T and PCC, as has been shown, but caution should be exercised when interpreting the images to avoid misinterpretations.

When capturing SE images a $10\,\mu s$ dwell time was generally used [75]. However some images are composites of images captured with significantly lower dwell times (e.g. Figure 5.1), in order to minimize charging artifacts [60]. Lower dwell

time reduces the image quality by decreasing the signal-to-noise ratio, but when several images are averaged the quality becomes comparable to images taken with longer dwell times [61]. This proved particularly useful when imaging the PCC samples. The porous surface created centers of localized charge, and images without bright lines resulting from charging were only successfully captured when averaging several images captured with low dwell times.

5.6 Further Work

The presence of larger fibers in combinations with cellulose nanofibrils may be a driver for flocculation of microcapsules, as evidenced by Figure 4.7. It follows that removing these large fibers from the process could greatly increase the likelihood of creating separate PEM microcapsules. Filtration may be one possibility. Further treatment of the pulp using carboxymethylation or TEMPO-oxidation - to increase charge density and whereby easing delamination - could be an alternative refinement [31].

Agglomeration and sedimentation of particles proved to be a hindrance for effectively measuring the system. Additives are commonly used to create smaller PCC particles [65, 66]. Using these smaller template particles could leading to more stable and measurable systems. If it were possible to more accurately measure ζ-potential, as would be the case with smaller particles, charge calculations could be used to more accurately establish the amount of PDADMAC and CNF-T need for charge reversal [25]. However, care should be taken to use particles of sufficient size, as problems are associated with wrapping stiff polyelectrolytes around particles with high curvature [73]. Further, the use of smaller template particles may not be worth pursuing if the flocculation issues are not remedied.

Vaterite is a metastable phase of $CaCO_3$ and any system is in constant state of change. In water vaterite will dissolve until the solution is saturated at the solubility of the polymorph. Working with solutions pre-saturated with Ca^{2+} at the solubility of vateriate may prevent some dissolution and make the surface more stable. However, this would likely pose some problems for the use of electrostatic forces in the formation PEMs [47, 68, 69]. Also of consequence are the indications that the adsorption of the first polyelectrolyte layer prevents further leakage of Ca^{2+} and ${CO_3}^{2-}$ [81]. Additional stabilization may not be necessary.

It becomes pertinent to ask if there are other more stable materials that could be chosen for the template particles. Though $CaCO_3$ was chosen for its use in papermaking [86], other particles may provide a better path to capsule formation. To wit, Ugelstad et al. (1980) developed a method of obtaining monosized polymer particles [89, 90]. Charged monodisperse polymer particles may provide greater

stability and control so as to make capsule formation possible.

Flow focusing is a common method for creating microbubbles [91–93]. Instead of using a PEM scheme to create capsules of CNF-T around a template particle, it might be possible to turn to a flow focusing method employing cationic surfactants. Another rather different approach to creating capsules, would be the use of spray drying. Spray drying has successfully been demonstrated for drying droplets of CNF suspensions [29, 94]. It could conceivably be possible to employ this technique to the problem of drying suspensions of CNF with added PCC particles. To determine the viability of these approaches, a literature review beyond the scope of this thesis would be required.

When it comes to characterizing the system viewing the samples before and after milling using SE has been the dominant method. Taking advantage of the contrast mechanisms of BSE may prove useful in future to study material contrast and thereby more precisely locate the different materials. However, the added difficulty of increased spot size would have to be considered [58]. STEM provides an indication of how TEM may be useful for providing visualization of the layered capsules. TEM would circumvent the need for a high energy ion beam, which could destroy the sample to the detriment of representative imaging. TEM is an established technique for the purpose of imaging microcapsules [32, 33, 95], but has some drawbacks in the form of difficult sample prep (very thin sample slices) and the use of high energy electrons. Polymers are beam sensitive, and TEM cannot be operated with the same low voltages as can SEM [58].

Further work should also be done on the freeze-drying of capsules. Though the efficaciousness of freeze-drying microcapsules with cooling in liquid N_2 has been proven, more work needs to be done as the capsules formation improves to investigate the drying behavior of CNF-T. The main aim is after all to establish whether the behavior found by Ottesen et al. (2017) is also present in PCC/CNF-T systems freed form the constraints of the paper matrix [20].

Chapter 6

Conclusion

A polyelectrolyte multilayer scheme was used in an effort to create capsules of CNF-T around $CaCO_3$ template particles, with the intent of studying the behavior of CNF-T upon drying of the capsules. It has become abundantly clear that the term microcapsule is at this juncture associated with wishful thinking. Firstly, the CNF-T adsorbing onto the PCC particles created very porous network structures, as apposed to a continuous layer. Secondly, large flocs formed around larger cellulose fibers, virtually eliminating the possibility of forming separate capsules. On the other hand, interaction between PCC, PDADMAC and CNF-T has been verified, and can be used as the basis for further exploration into their use in forming PEM capsules. As a first step, PDADMAC was found to coat PCC, providing a primed substrate for further layering with CNF-T. Freeze-drying using liquid N_2 as coolant, proved to be a suitable drying method for the finished product, and can in future - onces the capsule process has been optimized - be used as a foundation for continued study of the drying behavior of $CaCO_3$/CNF-T systems.

As a preamble to making microcapsules, the properties of PCC and CNF-T were studied. It was found that the PCC particles were very porous with an average diameter of around $6.3\,\mu\mathrm{m}$. CNF-T was determined to have an overlap concentration at around 0.17% (w/w), and concentrations of CNF-T should be kept well below this critical limit. It can however be concluded that the rheological properties are dependent on factors including CNF-T quality, source and measurement parameters and will warrant renewed investigation for each batch. The accuracy of calculating an appropriate ratio between PCC and CNF-T is aided by knowing the average fibril diameter of $2.7\,\mathrm{nm}$.

Changing the experimental parameters could yield significant improvement. Since it can be concluded that larger cellulose fibers play a role in the flocculation behavior, large flocs might be eliminated by using more homogeneous nanocellulose suspensions. This could in turn facilitate the possibility of using multiple layers of cellulose and creating denser shells. Other more radical possibilities include changing the material of the template particle or employing a completely different technique, such as flow focusing or spray drying. Some potential uses of CNF-T microcapsules have been considered, and further work on processing and property characterization of such capsules can be used to establish real-use potential.

Bibliography

[1] Michael Quirk and Julian Serda. *Semiconductor Manufacturing Technology*. Prentis Hall, 2001.

[2] James N. Culver et al. “Plant virus directed fabrication of nanoscale materials and devices”. In: *Virology* 479-480 (2015), pp. 200–212.

[3] Carissa M. Soto and Banahalli R. Ratna. “Virus hybrids as nanomaterials for biotechnology”. In: *Curr. Opin. Biotechnol.* 21.4 (2010), pp. 426–438.

[4] Tyler Meldrum et al. “A Xenon-Based Molecular Sensor Assembled on an MS2 Viral Capsid Scaffold”. In: *J. Am. Chem. Soc.* 132.17 (2010), pp. 5936–5937.

[5] Amy Szuchmacher Blum et al. “An Engineered Virus as a Scaffold for Three-Dimensional Self-Assembly on the Nanoscale”. In: *Small* 1.7 (2005), pp. 702–706.

[6] Robijn F. Bruinsma et al. “Viral Self-Assembly as a Thermodynamic Process”. In: *Phys. Rev. Lett.* 90.24 (2003), p. 248101.

[7] Marie Archer and Jinny Liu. “Bacteriophage T4 Nanoparticles as Materials in Sensor Applications: Variables That Influence Their Organization and Assembly on Surfaces”. In: *Sensors* 9.8 (2009), pp. 6298–6311.

[8] Chao Chen et al. “Packaging of Gold Particles in Viral Capsids”. In: *J. Nanosci. Nanotechnol.* 5.12 (2005), pp. 2029–2033.

[9] Kyoung Taek Kim et al. “Smart nanocontainers and nanoreactors”. In: *Nanoscale* 2.6 (2010), p. 844.

[10] Martin Fischlechner and Edwin Donath. “Viruses as Building Blocks for Materials and Devices”. In: *Angew. Chemie Int. Ed.* 46.18 (2007), pp. 3184–3193.

[11] Amy Szuchmacher Blum et al. “Molecular electronics based nanosensors on a viral scaffold”. In: *Biosens. Bioelectron.* 26.6 (2011), pp. 2852–2857.

[12] Maryam Zahedian et al. “Toward Virus-Like Surface Plasmon Strain Sensors”. In: *J. Phys. Chem. B* 120.26 (2016), pp. 5896–5906.

[13] Bodo D. Wilts, Iwan A.T. Schaap, and Christoph F. Schmidt. “Swelling and Softening of the Cowpea Chlorotic Mottle Virus in Response to pH Shifts”. In: *Biophys. J.* 108.10 (2015), pp. 2541–2549.

[14] Alain Dufresne. “Nanocellulose: a new ageless bionanomaterial”. In: *Mater. Today* 16.6 (2013), pp. 220–227.

[15] Stefaan De Koker, Richard Hoogenboom, and Bruno G. De Geest. “Polymeric multilayer capsules for drug delivery”. In: *Chem. Soc. Rev.* 41.7 (2012), p. 2867.

[16] Jiwei Cui et al. “Emerging methods for the fabrication of polymer capsules”. In: *Adv. Colloid Interface Sci.* 207.1 (2014), pp. 14–31.

[17] Alexey Yashchenok et al. “Polyelectrolyte multilayer microcapsules templated on spherical, elliptical and square calcium carbonate particles”. In: *J. Mater. Chem. B* 1.9 (2013), p. 1223.

[18] Claire S. Peyratout and Lars Dähne. “Tailor-Made Polyelectrolyte Microcapsules: From Multilayers to Smart Containers”. In: *Angew. Chemie Int. Ed.* 43.29 (2004), pp. 3762–3783.

[19] Alexei A. Antipov and Gleb B. Sukhorukov. “Polyelectrolyte multilayer capsules as vehicles with tunable permeability”. In: *Adv. Colloid Interface Sci.* 111.1-2 (2004), pp. 49–61.

[20] Vegar Ottesen et al. “Focused Ion Beam Tomography as a Means for Characterization of CNF in a Paper Matrix”. In: *Trans. 16Th Fundam. Res. Symp. Held Oxford Sept. 2017* (2017), pp. 595–610.

[21] Vegar Ottesen, Kristin Syveryd, and Øyvind Weiby Gregersen. “Mixing of cellulose nanofibrils and individual furnish components: Effects on paper properties and structure”. In: *Nord. Pulp Pap. Res. J.* 31.3 (2016), pp. 441–447.

[22] Akira Isogai, Tsuguyuki Saito, and Hayaka Fukuzumi. “TEMPO-oxidized cellulose nanofibers”. In: *Nanoscale* 3.1 (2011), pp. 71–85.

[23] Hayaka Fukuzumi et al. “Pore Size Determination of TEMPO-Oxidized Cellulose Nanofibril Films by Positron Annihilation Lifetime Spectroscopy”. In: *Biomacromolecules* 12.11 (2011), pp. 4057–4062.

[24] Fredrik Wenersson Brodin, Øyvind Weiby Gregersen, and Kristin Syverud. “Cellulose nanofibrils: Challenges and possibilities as a paper additive or coating material - A review”. In: *Nord. Pulp Pap. Res. J.* 29.1 (2014), pp. 156–166.

[25] G. B. Sukhorukov et al. “Stepwise polyelectrolyte assembly on particle surfaces: a novel approach to colloid design”. In: *Polym. Adv. Technol.* 767 (1998), pp. 759–767.

[26] Gleb B Sukhorukov et al. “Layer-by-layer self assebly of polyelectrolytes on colloidal particles”. In: *Colloids Surfaces A-Physicochemical Eng. Asp.* 137 (1998), pp. 253–266.

[27] Gleb B. Sukhorukov et al. “Hollow Polyelectrolyte Shells: Exclusion of Polymers and Donnan Equilibrium”. In: *J. Phys. Chem. B* 103.31 (1999), pp. 6434–6440.

[28] Jonathan Ø. Torstensen et al. “Preparation of cellulose nanofibrils for imaging purposes: comparison of liquid cryogens for rapid vitrification”. In: *Cellulose* (2018).

[29] Yucheng Peng, Douglas J. Gardner, and Yousoo Han. “Drying cellulose nanofibrils: in search of a suitable method”. In: *Cellulose* 19.1 (2012), pp. 91–102.

[30] Alain Dufresne. *Nanocellulose : from nature to high performance tailored materials*. Berlin: De Gruyter, 2012.

[31] Ali Naderi and Tom Lindström. “Rheological measurements on nanofibrillated cellulose systems: A science in progress”. In: *Cellul. Cellul. Deriv. Synth. Modif. Appl.* New York: Nova Science Publishers, 2015, pp. 187–204.

[32] Andreas Voigt et al. “Membrane Filtration for Microencapsulation and Microcapsules Fabrication by Layer-by-Layer Polyelectrolyte Adsorption”. In: *Ind. Eng. Chem. Res.* 38.10 (1999), pp. 4037–4043.

[33] F. Caruso. “Hollow capsule possessing through colloidal templating and self assembly”. In: *Chem. Eur. J.* 6.3 (2000), pp. 413–419.

[34] Guozhong Cao. *Nanostructures & Nanomaterials - Synthesis, Properties & Appplications*. London: Imperial College Press, 2004.

[35] Pratik Singh, Maria J. Gonzalez, and Marianne Manchester. “Depression with anxiety and atypical depression”. In: *Drug Dev. Res.* 67 (2006), pp. 23–41.

[36] S T Dubas and J B Schlenoff. “Factors controlling the growth of polyelectrolyte multilayers”. In: *Macromolecules* 32.24 (1999), pp. 8153–8160.

[37] Jielong Su et al. “Adsorption of cationic polyacrylamide at the celluloseâĂŞliquid interface: A neutron reflectometry study”. In: *J. Colloid Interface Sci.* 448 (2015), pp. 88–99.

[38] Tom Lindström and Christer Söremark. “Adsorption of cationic polyacrylamides on cellulose”. In: *J. Colloid Interface Sci.* 55.2 (1976), pp. 305–312.

[39] Ping Peng and Gil Garnier. “Effect of Cationic Polyacrylamide Adsorption Kinetics and Ionic Strength on Precipitated Calcium Carbonate Flocculation”. In: *Langmuir* 26.22 (2010), pp. 16949–16957.

[40] Rikard Lingström, Lars Wågberg, and Per Tomas Larsson. “Formation of polyelectrolyte multilayers on fibres: Influence on wettability and fibre/fibre interaction”. In: *J. Colloid Interface Sci.* 296.2 (2006), pp. 396–408.

[41] Lars Wågberg et al. “The Build-Up of Polyelectrolyte Multilayers of Microfibrillated Cellulose and Cationic Polyelectrolytes”. In: *Langmuir* 24.3 (2008), pp. 784–795.

[42] Bogdan V. Parakhonskiy et al. “Colloidal micro- and nano-particles as templates for polyelectrolyte multilayer capsules”. In: *Adv. Colloid Interface Sci.* 207.1 (2014), pp. 253–264.

[43] Alexei A. Antipov et al. “Carbonate microparticles for hollow polyelectrolyte capsules fabrication”. In: *Colloids Surfaces A Physicochem. Eng. Asp.* 224.1-3 (2003), pp. 175–183.

[44] Andrew T. Horvath et al. “Diffusion of Cationic Polyelectrolytes into Cellulosic Fibers”. In: *Langmuir* 24.19 (2008), pp. 10797–10806.

[45] Krister Holmberg et al. *Surfactants and Polymers in Aqueous Solutions*. 2nd. Chichester: Wiley, 2003.

[46] Paul C. Painter and Michael M. Coleman. *Fundamentals of Polymer Science*. 2nd. CRC PressLLC, 1997.

[47] Paul C. Hiemenz and Raj Rajagopalan. *Principles of Colliod and Surface Chemistry*. 3rd. Boca Raton, 1997.

[48] Martin A. Hubbe et al. “Rheology of nanocellulose-rich aqueous suspensions: A review”. In: *BioResources* 12.4 (2017), pp. 9556–9661.

[49] Alan Rawle. “The importance of particle sizing to the coatings industry Part 1 : Particle size measurement”. In: *Adv. Colour Sci. Technol.* 5.1 (2002), pp. 1–12.

[50] David Brandon and Wayne D Kaplan. “Optical Microscopy - Microstructural Characterization of Materials”. In: *Microstruct. Charact. Mater.* Chichester: Wiley, 2008, pp. 123–177.

[51] Terrence Allen. *Particle Size Measurement*. 4th. Cornwall: Chapman and Hall, 1990.

[52] Wolfram Hergert and Thomas Wriedt. *The Mie Theory: Basics and Applications*. Berlin: Springer, 2012.

[53] Franz J. Giessibl. "Advances in atomic force microscopy". In: *Rev. Mod. Phys.* 75.3 (2003), pp. 949–983.

[54] Greg Haugstad. *Atomic Force Microscopy: Understanding Basic Modes and Advanced Applications*. Somerset: Wiley, 2012.

[55] Gerhard Hübschen et al. *Materials Characterization Using Nondestructive Evaluation (NDE) Methods*. Elsevier Ltd, 2016.

[56] Catherine Bréchignac, Philippe Houdy, and Marcel Lahmani. *Nanomaterials and Nanochemistry*. Heidelberg: Springer, 2007.

[57] C. Dupas, P. Houdy, and M. Lahmani. *Nanoscience: Nanotechnologies and Nanophysics*. Heidelberg: Springer, 2007.

[58] R.F. Egerton. *Physical Principles of Electron Microscopy: An Introduction to TEM, SEM and AEM*. 2nd. 2016.

[59] Anjam Khursheed. "Ultimate resolution limits for scanning electron microscope immersion objective lenses". In: *Optik (Stuttg).* 113.2 (2002), pp. 67–77.

[60] Dc Joy and Cs Joy. "Low voltage scanning electron microscopy". In: *Micron* 27.3-4 (1996), pp. 247–263.

[61] Joseph I Goldstein et al. *Scanning Electron Microscopy and X-Ray Microanalysis*. 4th. New York: Springer, 2018.

[62] Stephen J. Pennycook and Peter D. Nellist. *Scanning Transmission Electron MicroscopyâĂŤImaging and Analysis*. New York: Sprint, 2011.

[63] Nan Yao. *Focused Ion Beam Systems: Basics and Applications*. Cambridge University Press, 2007.

[64] Lucille a. Giannuzzi and Fred a. Stevie. *Introduction To Focused Ion Beams - Intrumentation, Theory, Techniques and Practice*. New York: Springer, 2005.

[65] Daria B. Trushina, Tatiana V. Bukreeva, and Maria N. Antipina. "Size-Controlled Synthesis of Vaterite Calcium Carbonate by the Mixing Method: Aiming for Nanosized Particles". In: *Cryst. Growth Des.* 16.3 (2016), pp. 1311–1319.

[66] D. B. Trushina et al. “Size control and structure features of spherical calcium carbonate particles”. In: *Crystallogr. Reports* 60.4 (2015), pp. 570–577.

[67] Vegar Ottesen et al. “Viability and properties of roll-to-roll coating of cellulose nanofibrils on recycled paperboard”. In: *Nord. Pulp Pap. Res. J.* 32.2 (2017), pp. 179–188.

[68] Lars-erik Enarsson and Lars Wågberg. “Polyelectrolyte Adsorption on Thin Cellulose Films Studied with Reflectometry and Quartz Crystal Microgravimetry with Dissipation Polyelectrolyte Adsorption on Thin Cellulose Films Studied with Reflectometry and Quartz Crystal Microgravimetry with”. In: *Society* 10.November 2008 (2009), pp. 134–141.

[69] Bo Wu et al. “Formation of Polyelectrolyte Multilayers by Flexible and Semiflexible Chains”. In: *J. Phys. Chem. B* 116.10 (2012), pp. 3106–3114.

[70] Min Young Lee et al. “Target-specific gene silencing of layer-by-layer assembled gold-cysteamine/siRNA/PEI/HA nanocomplex”. In: *ACS Nano* 5.8 (2011), pp. 6138–6147.

[71] Gordon Aylward and Tristan Findlay. *SI Chemical Data*. 6th. 2008.

[72] Galina Rodionova et al. “TEMPO-Mediated Oxidation of Norway Spruce and Eucalyptus Pulps: Preparation and Characterization of Nanofibers and Nanofiber Dispersions”. In: *J. Polym. Environ.* 21.1 (2013), pp. 207–214.

[73] A Elbakry. “Layer-by-layer assembled gold nanoparticles for siRNA delivery”. In: *Nano Lett.* 9.5 (2009), pp. 2059–2064.

[74] Dmitry V. Volodkin et al. “Matrix Polyelectrolyte Microcapsules: New System for Macromolecule Encapsulation”. In: *Langmuir* 20.8 (2004), pp. 3398–3406.

[75] Erik Dobloug Roede. “FIB/SEM Characterization of Paper Materials”. MA thesis. NTNU, 2016.

[76] Elsa Lasseuguette, Denis Roux, and Yoshiharu Nishiyama. “Rheological properties of microfibrillar suspension of TEMPO-oxidized pulp”. In: *Cellulose* 15.3 (2008), pp. 425–433.

[77] Ali Naderi, Tom Lindström, and Jonas Sundström. “Carboxymethylated nanofibrillated cellulose: rheological studies”. In: *Cellulose* 21.3 (2014), pp. 1561–1571.

[78] Randal L. Shogren et al. “Preparation and characterization of cellulose gels from corn cobs”. In: *Carbohydr. Polym.* 86.3 (2011), pp. 1351–1357.

[79] Jens-Petter Andreassen, Ralf Beck, and Margrethe Nergaard. “Biomimetic type morphologies of calcium carbonate grown in absence of additives”. In: *Faraday Discuss.* 159 (2012), p. 247.

[80] Nora H. de Leeuw and Stephen C. Parker. “Surface Structure and Morphology of Calcium Carbonate Polymorphs Calcite, Aragonite, and Vaterite: An Atomistic Approach”. In: *J. Phys. Chem. B* 102.16 (1998), pp. 2914–2922.

[81] Dmitry V. Volodkin, Natalia I. Larionova, and Gleb B. Sukhorukov. “Protein Encapsulation via Porous CaCO 3 Microparticles Templating”. In: *Biomacromolecules* 5.5 (2004), pp. 1962–1972.

[82] Jens-Petter Andreassen. “Formation mechanism and morphology in precipitation of vateriteâĂŤnano-aggregation or crystal growth?” In: *J. Cryst. Growth* 274.1-2 (2005), pp. 256–264.

[83] Reina Tanaka et al. “Determination of nanocellulose fibril length by shear viscosity measurement”. In: *Cellulose* 21.3 (2014), pp. 1581–1589.

[84] Andrew T. Horvath et al. “Adsorption of highly charged polyelectrolytes onto an oppositely charged porous substrate”. In: *Langmuir* 24.15 (2008), pp. 7857–7866.

[85] Jani Salmi, Monika Österberg, and Janne Laine. “The effect of cationic polyelectrolyte complexes on interactions between cellulose surfaces”. In: *Colloids Surfaces A Physicochem. Eng. Asp.* 297.1-3 (2007), pp. 122–130.

[86] Christopher J. Biermann. *Handbook of Pulping and Papermaking*. 2nd. California: Academic Press Inc, 1996.

[87] Praveena Raj et al. “Microfibrilated cellulose as a model for soft colloid flocculation with polyelectrolytes”. In: *Colloids Surfaces A Physicochem. Eng. Asp.* 516 (2017), pp. 325–335.

[88] Jingquan Han et al. “Self-Assembling Behavior of Cellulose Nanoparticles during Freeze-Drying: Effect of Suspension Concentration, Particle Size, Crystal Structure, and Surface Charge”. In: *Biomacromolecules* 14.5 (2013), pp. 1529–1540.

[89] J. Ugelstad et al. “Swelling of oligomer-polymer particles. New methods of preparation”. In: *Adv. Colloid Interface Sci.* 13.1-2 (1980), pp. 101–140.

[90] John Ugelstad et al. “Preparation and Biochemical and Biomedical Applications of N e w Monosized Polymer Particles *”. In: *Polym. Int.* 30 (1993), pp. 157–168.

[91] K. P. Pancholi et al. “Novel methods for preparing phospholipid coated microbubbles”. In: *Eur. Biophys. J.* 37.4 (2008), pp. 515–520.

[92] Sally A. Peyman et al. “Expanding 3D geometry for enhanced on-chip microbubble production and single step formation of liposome modified microbubbles”. In: *Lab Chip* 12.21 (2012), p. 4544.

[93] Rajeev Parmar and Subrata Kumar Majumder. “Microbubble generation and microbubble-aided transport process intensificationâĂŤA state-of-the-art report”. In: *Chem. Eng. Process. Process Intensif.* 64 (2013), pp. 79–97.

[94] Yucheng Peng, Yousoo Han, and Douglas J Gardner. “Spray-Drying Cellulose Nanofibrils : Effect of Drying Process Parameters on Particle Morphology”. In: *Wood Fiber Sci.* 44.4 (2012), pp. 1–14.

[95] Edwin Donath et al. “tion are fabricated by stepwise adsorption of oppositely charged polyelectrolytes onto melamin resin templates which are subsequently solubilized . P olyelectrolyte shells with controlled thickness and composi- T he confocal micrograph of a shell that is”. In: *Angew. Chemie Int. Ed.* 37.16 (1998), pp. 2201–2205.

Appendix

A risk assessment of the work can be found in the internal systems of the Department of Chemical Engineering (NTNU). Reference ID: 22406

Table 1: Viscosity (η) values for CNF-T averaged over 12 measurements for each concentration.

Concentration [wt%]	**Viscosity (η) [Pa · s]**	**SD [Pa · s]**
0.05	0.0042	0.0001
0.07	0.0069	0.0001
0.10	0.0149	0.0001
0.12	0.0212	0.0001
0.13	0.0263	0.0003
0.15	0.0438	0.0004
0.17	0.0518	0.0007
0.19	0.0825	0.0008
0.20	0.1039	0.0007
0.21	0.1154	0.0010
0.23	0.1532	0.0012
0.24	0.1772	0.0015
0.25	0.2097	0.0033
0.28	0.2949	0.0123
0.30	0.3778	0.0146
0.33	0.4207	0.0118
0.35	0.6027	0.0480
0.40	0.9563	0.0597
0.50	2.1441	0.1841
0.85	10.7909	0.7715

Table 2: p-values and W (also known as U) from statistical analysis of the CNF-T fibril diameters obtained from AFM micrographs. Diameter differences between drying at 70 °C or 90 °C were analyzed. Additionally, the temperatures were comparisons to samples used by Ottesen et al. [67]. The statistical test use was a Wilcoxon rank-sum test, as the data cannot be assumed to be normally distributed.

70 °C and 90 °C		**70 °C and Ottesen et al.**		**70 °C and Ottesen et al.**	
p-value	W	p-value	W	p-value	W
0.4341	4866	$6.957 \cdot 10^{-9}$	4139	$2.161 \cdot 10^{-12}$	5771